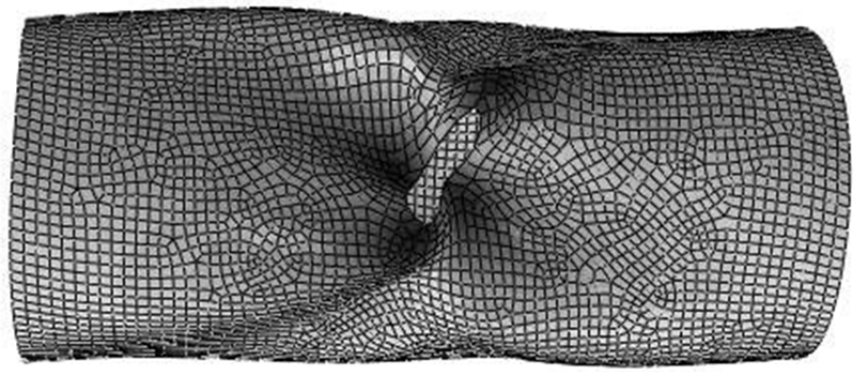

Figure 74 - Bleeder Carbon Buckled Shape Without Reduced Stiffness

Models With Damage Around Hole

When a hole is cut into a composite the tows cut by the hole become discontinuous and lose stiffness until developed by the matrix and the surrounding tows. Further, holes were cut with a hole saw, the same device used for cutting filling holes for concrete filling, which damages the surrounding matrix. The initial model with the hole ignored stiffness loss of the composite around the hole caused by inadequate development length and a damaged composite. A simplified approach was used to generate new material properties for a region immediately surrounding the hole of a certain width. This area had a 50% modulus reduction (E_x, E_θ, and G_{xy}) to reflect a linear change in modulus from the damaged edge (0 stiffness) to the full moduli in the body of the tube. At the damaged edge, the moduli will not be zero; the matrix will retain some of its stiffness. All properties are reduced evenly, although the shear modulus and off-axis modulus will develop more rapidly than the fiber direction modulus because they are more dependent on matrix properties. The radial and longitudinal moduli are a combination of all material direction moduli. The fiber direction modulus is much higher than the off-axis modulus, a uniform reduction was taken for all properties. The width of the surrounding area, from the physical hole to the edge of the reduced property region, was chosen to force the model to produce the experimental average buckling load, as shown in Table 31

This test report shall not be reproduced, except in full, without the written approval of
the AEWC Advanced Structures & Composites Center.

Table 31 Length Convergence for Reduced Stiffness Area

Soft Region Width	BC Small	DC Small	DC Large
Experimental	48.9	74.3	47.6
No Reduced Stiffness	124	207	70.2
0.50in	69.4	116	58.5
0.94in	-	-	**47.5**
1.00in	57.6	95.3	46.2
1.5in	50.5	82.5	-
1.70in	**48.8**	-	-
1.85in	47.7	77.5	-
2.20in	46	**74.7**	-

The width of the damaged region was also compared with the equation for shear lag of a tow in resin, the development length of a tow in neat resin, where V is volume fraction, η is the length modification factor (Equation 22
), l is the tow length, r_f is fiber radius, and all other values are shear and longitudinal moduli for the fibers f or the matrix m (Nairn, 1997). When the equation reaches 90% of the fiber modulus, as given by Equation 23
, the fiber is considered fully developed. For the carbon development occurs at 0.91in, 0.984in for the glass. These values compare reasonably with the optimal lengths of the damaged region of 0.94in to 2.20in reported in Table 31.

$$\eta = \left(\sqrt{\left(\frac{2}{r_f^{\,2} E_{af} E_{am}} \right) \left[\frac{E_{af} V_f + E_{am} V_m}{\frac{V_m}{4G_{af}} + \frac{1}{2G_{am}} \left(\left(\ln\left(\frac{1}{V_1} \right) - 1 - \frac{V_m}{2} \right) / V_m \right)} \right]} \right) \qquad \text{Equation 22}$$

$$E_f = E_{af} \frac{2(1 - \tanh(l\eta))}{l\eta} \qquad \text{Equation 23}$$

To assign material properties around the hole, a larger hole had to be modeled into the composite using the same method as for the smaller hole. The Area between the larger hole and the smaller hole were then joined to form a new section in the part using the merge command in the ABAQUS assembly module. The new reduced region, when meshed, appears in Figure 75. Because the tube section with a portion removed and the

This test report shall not be reproduced, except in full, without the written approval of
the AEWC Advanced Structures & Composites Center.

ring were stored as separate regions with different properties in the same part, no tie constraints or contact were needed for this analysis.

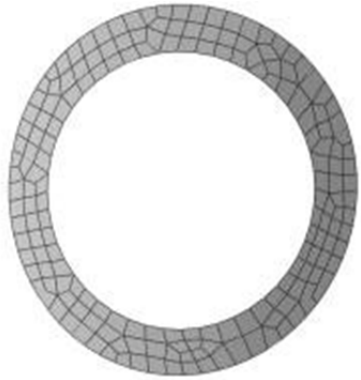

Figure 75 - Meshed Reduced Area Around Hole

The new model produced a lower capacity than the previous model without the reduced ring around the hole. The buckled shape alters substantially. Figure 76 shows the buckled shape and the predicted buckling shape. In both cases the area above the hole rotates inward and the material on the edges of the hole, near the mid height of the hole, buckles outward and undergoes the maximum deformation.

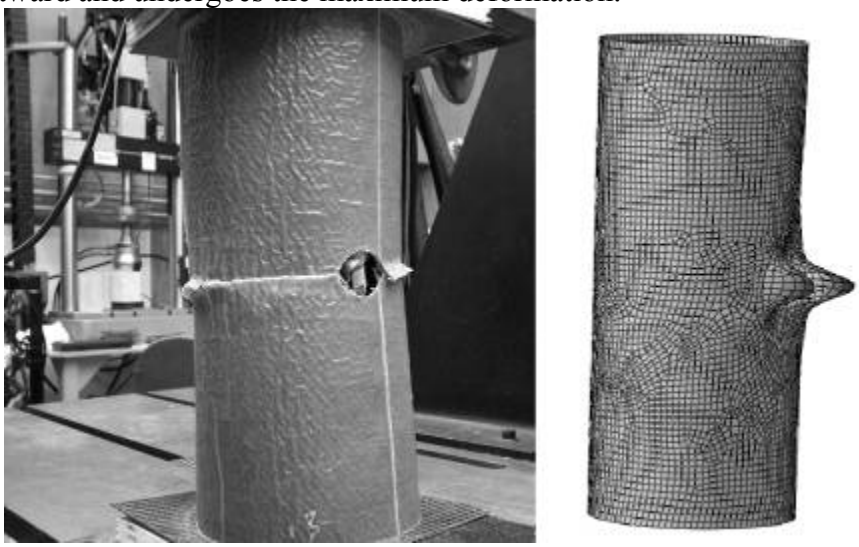

Figure 76 - Comparison of Model to Actual Buckled Shape

Imperfections in Tubes With Holes

Tubes with holes were just as likely to have unbalanced loading and irregular geometries as specimens without holes. Unlike solid specimens the hole was a local weak spot and

This test report shall not be reproduced, except in full, without the written approval of
the AEWC Advanced Structures & Composites Center.

the direction of curvature or uneven loading affects the load path relative to the hole, affecting the buckling capacity. As seen in the previous sections, the hole is a severe weakness in the model and specimen and it was important to determine whether other geometric imperfections played a significant role in buckling capacity.

Effect of Unbalanced Loading in Tubes with Holes

Six models were run for each material type for an unbalanced loading case, and the results of the analysis are summarized in Table 32. The unbalanced load varied linearly based on angular location. These models put the peak load directly over the hole, diametrically against the hole, and at a 90-degree angle from the hole. Loads applied to the top and bottom surface of the tube were equal and opposite and always applied in the plane of the cylinder wall. Applying the maximum load above the position of the hole caused a dramatic loss in capacity similar to that seen in the low outliers of the experimental results for the carbon bleeder specimens with holes. Plywood end caps crushed (from experimental observation) near 6.74kip; any specimen that failed at or below 6.74kip did not have an opportunity to damage the plate and redistribute the load. Both the bleeder carbon with a small hole and the double carbon with the large hole were, according to the model, capable of failing under a lopsided load prior to plywood cap failure. Figure 77 shows the effect on buckled shape of moving the concentrated load to different faces of the cylinder.

Table 32 Capacity of Models With Holes and Unbalanced Loads in kips

TYPE	DC small	BC small	DC large
Even Load	16.8	11.0	10.7
Partial Unbalance Over the Hole	12.7	9.67	8.30
Partial Unbalance Off the Hole	24.5	16.9	13.9
Partial Unbalance Side of Hole	17.7	12.1	10.1
Full Unbalance Over the Hole	10.1	6.77	5.89
Full Unbalance Off the Hole	42.0	27.0	33.7
Full Unbalance Side of Hole	16.6	11.4	9.22

This test report shall not be reproduced, except in full, without the written approval of
the AEWC Advanced Structures & Composites Center.

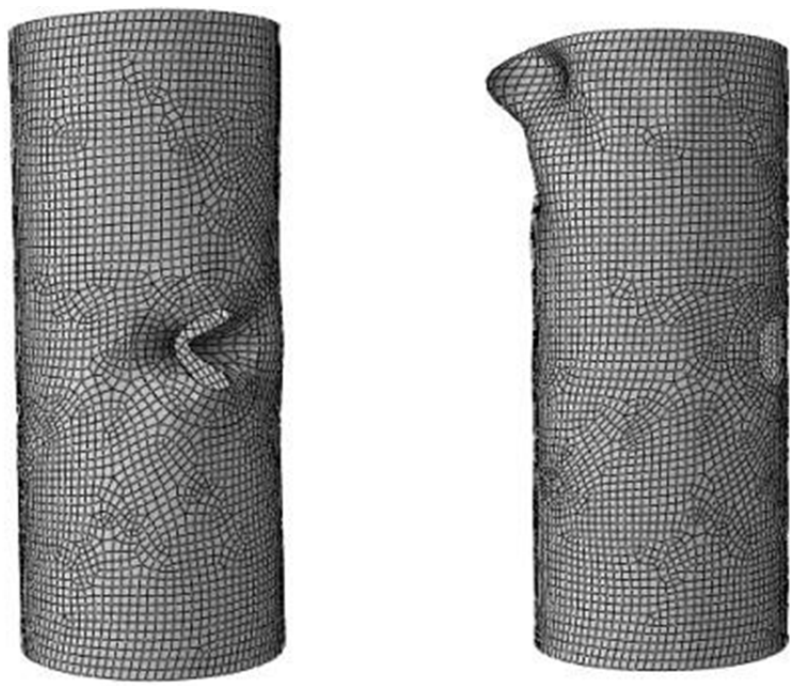

Figure 77 - Small Hole Double Carbon Model with Different Load Locations

Effect of Geometric Imperfections in Tubes With Holes

The models with holes were perturbed into the same geometric irregularities as the cylinder models without holes. Asymmetric model variations (ellipse, single curvature, double curvature, and arc) depend on the relative position of the hole to the geometry of the cylinder. Single curvature and arc models have a front, rear, and side model and the double curvature and ellipse each have a front and side model (the front and rear are symmetric for these models). In general, deformities were less important for buckled shape or failure load in models with holes because the hole was the dominant failure for most models. Asymmetric models that either concentrated or dispersed the load in the region around the hole had an effect, but the percent change was generally larger for the cylinder without holes than the holed cylinder when deformed. Table 33 contains the capacity of all tested geometric imperfections.

The hourglass, bulge, double curvature, minor axis ellipse, and single curvature 90 degrees from hole all have negligible reductions versus the perfect cylinder – less than 5% increase or decrease even with large perturbations. The major axis ellipse produced a sizeable decrease with a large change in radius, but based on experimental testing discussed in Bend Testing of Hollow FRP Tubes, it seems unlikely that this level of ellipticity will ever be reached during filling. Single curvature and arc curvature can

This test report shall not be reproduced, except in full, without the written approval of
the AEWC Advanced Structures & Composites Center.

produce significant changes in the capacity of the cylinder. With a hole on the outward curving face of the single curvature shape the capacity increased because the load path moved away from the defect. With the hole on the inward curving face capacity is reduced. This phenomenon was similar to the uneven loading case, only the results were less severe. The arc shape produces significantly lower results whether the hole was located on the front, rear or side of curve – not the anticipated result. All material models shared this result suggesting that the hole adversely affected the capacity of the arched shell. The small reduction for most defects explains the low COVs from the experimental loads (8.1% bleeder carbon, 5.7% small hole, and 7.5% big hole double carbon).

This test report shall not be reproduced, except in full, without the written approval of
the AEWC Advanced Structures & Composites Center.

Table 33 Failure Load in kips of Models with Hole and Geometric Imperfection

Type	DC small	BC small	DC large
Experimental	16.8	11.0	10.7
Non-Deformed	16.8	11.0	10.8
Hourglass - 0.02in	16.8	11.1	11.0
Hourglass – 0.06in	16.8	11.2	11.2
Hourglass - 0.10in	16.8	10.9	10.6
Bulge - 0.02in	16.7	10.8	10.4
Bulge - 0.06in	16.6	10.7	10.2
Bulge - 0.10in	16.8	11.0	10.7
Single Curvature Front - 0.10in	16.9	11.2	10.8
Single Curvature Front - 0.06in	17.6	11.8	11.2
Single Curvature Front - 0.50in	17.5	11.4	10.7
Single Curvature Back - 0.10in	18.8	12.0	10.9
Single Curvature Back - 0.06in	19.9	12.7	11.3
Single Curvature Back - 0.50in	16.0	10.5	10.4
Single Curvature Side - 0.10in	14.5	9.49	9.76
Single Curvature Side - 0.06in	12.9	8.43	9.01
Single Curvature Side - 0.50in	16.8	11.0	10.7
Double Curvature Front - 0.10in	16.6	10.9	10.7
Double Curvature Front - 0.06in	16.5	10.7	10.6
Double Curvature Front - 0.50in	16.8	11.0	10.7
Double Curvature Side - 0.10in	16.7	10.9	10.7
Double Curvature Side - 0.06in	16.7	10.7	10.8
Double Curvature Side - 0.50in	16.9	11.0	10.4
Ellipse Major - 0.10in	17.0	11.0	9.82
Ellipse Major - 0.06in	16.9	10.9	9.06
Ellipse Major - 0.50in	16.6	10.9	10.9
Ellipse Minor - 0.10in	16.2	10.7	11.1
Ellipse Minor - 0.06in	15.8	10.5	11.3
Ellipse Minor - 0.50in	15.9	10.7	9.42
Arc Side - 0.10in	16.3	11.0	9.73
Arc Side - 0.06in	17.1	11.7	9.98
Arc Side - 0.50in	15.3	10.2	9.24
Arc Front - 0.10in	14.1	9.42	9.40
Arc Front - 0.06in	13.0	8.61	9.85
Arc Front - 0.50in	16.5	10.9	9.28
Arc Back - 0.10in	17.6	11.5	9.47
Arc Back - 0.06in	18.5	12.0	9.91

This test report shall not be reproduced, except in full, without the written approval of
the AEWC Advanced Structures & Composites Center.

Arc Back - 0.50in	16.8	11.0	10.7

Case Study, Caribou, Maine Bridge

A bridge planned for construction during summer, 2011 in Caribou, Maine is being built with a longer span and larger span to depth ratio than previous bridges, meaning that moments would potentially be higher than previous bridges and this bridge would be closer to critical load during filling. This chapter contains the modified finite element shell model for the new shell lay-up. In this circumstance the model was predictive; no testing was performed on this geometry and fiber construction.

Model Input Parameters

The shell for this model is identical to the Belfast Bridge that is described in Walton (2011); material properties use a 1-layer per braid model, adhering to principals from Lamina with One Orthotropic Layer per Braid. Material properties for the 14.76in diameter Caribou model are in Table 34. The cylinder in the model had length 36.0in, larger than the 15.0in length used in previous modeling, to keep a consistent diameter to length ratio. Two models were constructed: one with a 2.50in hole, to compare with stress at the apex, and one without a hole to compare with stress at the footing (peak stress); no perturbations were applied to either model. In the model with hole a reduced property region was created around the hole. As with previous models, stiffness was reduced by 50% (E_x, E_y, G_{xy}) for a length of 1.10in in all directions. The same methods as described previously were used for connecting the reduced properties section with the solid cylinder. The model was meshed with larger elements than previous, 0.512in per side, keeping approximately the same number of total elements in the model.

Table 34 Caribou Bridge Material Input Parameters

Property	Carbon	E-Glass
Angle (Degrees)	16	76
Thickness (in)	.039	.038
E_1 (Ksi)	8990	1200
E_2 (Ksi)	1000	4150
v_{12}	0.977	0.139
G_{12} (Ksi)	1090	631

This test report shall not be reproduced, except in full, without the written approval of the AEWC Advanced Structures & Composites Center.

Model Results

Buckling capacity for the two models are displayed in Table 35 results are given in stress (ksi), instead of force (kips), the reported quantity for all previous buckling models. For pure axial loads, stress is constant in the cross section, for combined bending moment and axial load the stress varies in the cross section and the peak stress (combined) from the load model is compared to the model buckling stress (axial). Model results indicate a large reduction in buckling capacity when the hole is included, as seen in previous models. As the hole implemented in this arch is smaller, relative to length and diameter, to previous holes, the reduction in capacity is not as dramatic as that for previous holes. The model results are presented directly from ABAQUS, without any additional reduction. For previous results the double carbon experimental buckling average was 45% of the ABAQUS model prediction, so confidence on the accuracy of the model without holes is low. Applying large perturbations to the model is one potential approach toward getting a more accurate model. Figure 78 and Figure 79 show the lowest eigenvalue buckled shape for the models. The model without a hole is very different from previous buckling modes; shape change is localized to the central portion of the cylinder instead of the more uniform buckling mode of smaller diameter models.

Table 35 Caribou Bridge, Model Predicted Buckling Stress

	No Hole	**With Hole**
Model Buckling Stress (Ksi)	16.7	7.40

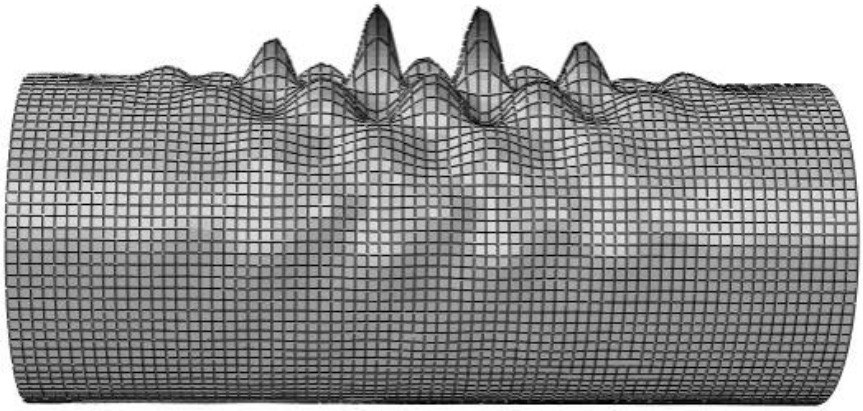

Figure 78 - Caribou Cylinder Without Hole

This test report shall not be reproduced, except in full, without the written approval of
the AEWC Advanced Structures & Composites Center.

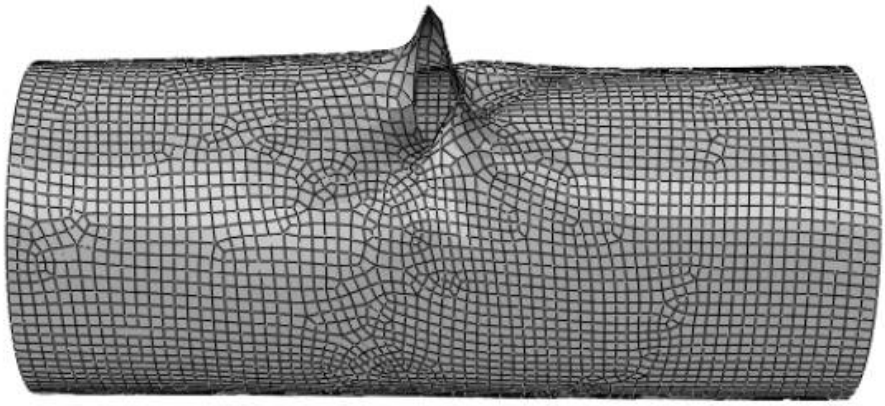

Figure 79 - Caribou Cylinder With Hole

Conclusion

Finite element shell models were used to perform eigenvalue buckling analyses and estimate the buckling capacity of short axial compression cylinders. The models were created to reflect actual test specimens and determine what factors influenced the buckled shape and buckling load. Several element types and material idealizations were considered, and mesh refinement was also addressed. In general, model-predicted buckling loads were higher than experimental buckling loads, and unbalanced loading and geometric defects were implemented to reduce capacity and more accurately compare to tests.

Of the geometric defects considered, only the extreme arc and single curvature defects were able to reduce the load from the perfect model to the experimental buckling load. Most specimens were closer to the perfect model, yet they still failed at a reduced load. Only cylinder global defects were considered; local fiber inconsistencies including tow size and tow overlap were ignored. These micro defects, in conjunction with a combination of the less extreme diameter and curvature defects likely account for the variability in the experimental load and the difference between the experimental load and the theoretical load.

Models with holes predicted buckling at loads close to experimental buckling loads for specimens with holes. Models with holes were minimally affected by diameter defects, indicating that the presence of the hole dominated response, and local geometric defects were unlikely to reduce buckling capacity further. The only defects that affected the capacity of models with holes were ones that rapidly changed the curvature near mid height – the single curvature and arc models. By extension, local defects including tow thickness and stiffness are expected to minimally affect the capacity of models/specimens

This test report shall not be reproduced, except in full, without the written approval of
the AEWC Advanced Structures & Composites Center.

with holes. The hole was the dominant defect and unless the model/specimen was unevenly loaded or curved, there is expected to be good agreement between the model-predicted and experimentally measured buckling loads.

This test report shall not be reproduced, except in full, without the written approval of
the AEWC Advanced Structures & Composites Center.

BEND TESTING OF HOLLOW FRP TUBES

Concrete filled FRP arches are designed as cast in place members where the FRP skin serves as the formwork for the curing concrete and the tensile reinforcing for the completed arch. When the concrete is first pumped into the arch it is a fluid, meaning that it contributes no strength or stiffness to the arch while it adds self-weight. The FRP arches made at the AWEC have a short height versus span and are formed around a circular section; this results in combined axial compression and bending. The FRP skin of the arch must carry this bending and axial compression load alone. Even if temporary shoring can be installed to support the arch during filling, it could cause large concentrated loads on the arch shell, which could lead to premature failure due to the low stiffness of the hollow FRP shell when loaded in the direction of cross-sectional radius.

When a hollow shape is subjected to a bending moment, there is a distortional effect caused by bending stress and curvature that alters the cross sectional shape. For a circular cross section the distorted shape can be approximated by an ellipse, where the radius perpendicular to the axis of bending decreases. This reduces the section modulus (bending resistance) and buckling capacity (see Modeling Buckling for a Hollow Cylinder, shell element modeling of cylinders) for an actual beam or arch. This phenomenon was first analyzed by Brazier (1927) and is sometimes referred to as Brazier's effect. Brazier used many simplifications and ignored higher order terms in approximating values, but later research (Kedward, 1978 and Tatting, 1997) has shown that Brazier's approximations for bending moment and radius change were reasonably accurate. Brazier (1927) and Tatting (1997) both noted that local buckling modes exist that are driven by geometry and stiffness and can result in beams failing in bifurcation buckling prior to the reaching the maximum bending moment and maximum radius reduction of 22% proposed by Brazier. Prior research assumes a geometrically perfect beam and isotropic (Brazier) or orthotropic (Kedward and Tatting) material, and deviation from these properties can reduce the collapse moment, giving smaller radius change at failure.

The two goals of the testing reported in this chapter were to find the failure stress of a hollow FRP shell in bending and to find how much cross sectional distortion occurred before failure. To avoid point source loading and mimic the effect of wet concrete, fluid (water) was used as a loading source. In some tests, bending stiffness was measured by applying a known weight near mid span and measuring mid span deflections.

Specimen Fabrication and Material Properties for Bending

Fluid filled bend tests occurred in October 2009 and June 2010. Each test used tubes composed of different material properties and having different geometries. For clarification the three tested glass tubes will be referred to as tubes G1, G2, G3 while the

This test report shall not be reproduced, except in full, without the written approval of
the AEWC Advanced Structures & Composites Center.

six tested carbon fiber tubes will be referred to as tubes C1 – C6. Carbon fiber specimens that did not fail during testing were tested a second time after being rotated 90 degrees to get additional results from the same number of specimens; tests are labeled 'top' or 't' for the initial orientation and 'side' or 's' for the alternate orientation. The basic characteristics of the specimens are summarized in Table 36. Specimens built for testing in October were 11.8in diameter glass tubes with length 358.27in to 366.14in. Tubes were constructed of a diameter constraint e-glass (+/- 81 degrees, 0.043in) and a structural longitudinal e-glass (+/-30 degrees, 0.016in), and all three tubes were nominally identical although tube G1 was subject to incomplete vacuum after infusion making one side resin rich and the other side resin poor. Specimens for testing in June 2010 were 6.50in diameter carbon tubes with lengths of 433.04in to 472.44in. The fiber architecture (fiber angle, infused thickness) was diameter constraint e-glass (+/-81 degrees, 0.035in), one (tubes C1-C4) or two (tube C6) layers of structural carbon fiber (+/-22 degrees, 0.027in per layer), and for specimen C5, one layer of structural carbon fiber (+/-22 degrees, 0.027in) and a 0.032in thick homogenous polyester mat outer bleeder layer. Specimen and layer thicknesses were measured after undamaged sections of the tubes were cut for compression testing.

Table 36 Bend Testing Matrix

Diameter	Single Carbon	Double Carbon	Carbon Bleeder	Outer Glass
6.50in	C1-C4	C6	C5	0
11.8in	0	0	0	G1-G3

Tubes C2-C6 were loaded with a single 51lb sand bag to produce a local distributed load centered at 12.0in from mid span (while the mid span deflection was being measured) to find the bending stiffness *EI*. Table 37 contains the measured bending stiffness and the theoretical bending stiffness for the carbon fiber tubes. Theoretical bending stiffness was based on Classical Lamination Theory (CLT) and micromechanics properties for the carbon fibers, glass fibers, polyester mat fibers, and vinyl ester matrix, see Material Assumptions for material model assumptions.

This test report shall not be reproduced, except in full, without the written approval of
the AEWC Advanced Structures & Composites Center.

Table 37 Elastic Modulus from Sand Tests

	SC	BC	DC
Experimental E_x (Ksi)	5920	4210	8500
COV (%)	5.43	5.77	3.03
Predicted E_x (Ksi)	5740	4080	7180
Percent Difference	3.00	3.17	15.49

Test Setup

Water fill testing was performed outside to avoid water spills indoors after tube failure. shows the test setup used for the 6.50in diameter specimens (the setup for 11.8in specimens was similar). Reinforced concrete supports, 29.9in cubes, were positioned 359.84in on center on level asphalt or on concrete blocks such that the center of both supports had the same elevation. The concrete cube was topped by a rocker platform restrained to allow only in-plane rotation and hardwood saddles to prevent the tube from displacing in any direction, as in Figure 81. Beams were simply supported. The larger diameter tubes sat snugly in the saddles while the smaller diameter tubes were strapped into the saddles with neoprene padding because the same saddles were used for both tube diameters. To prevent water from spilling out of the ends of the tubes inflatable rubber plugs were tightened into position over the supports for all tubes during testing. Wooden stands straddled the tube at five evenly spaced intermediary points along the length of the tube to hold instrumentation.

This test report shall not be reproduced, except in full, without the written approval of
the AEWC Advanced Structures & Composites Center.

Figure 80 - Test Setup for 6.50in Diameter Specimens

The water fill rate was assumed to be constant for the duration of a single test. For the 11.8in diameter tests the fill time for a bucket (45.19lb capacity) was measured three times, twice prior to test, and once after test, to establish a flow rate. Flow rate varied by less than 1 second for all tests on a 11.8in tube corresponding to COVs <1%. Tube G3 – tested on a different day than tubes G1 and G2 – had a statistically significant difference in fill time, and a different fill time was used. For the 6.50in diameter specimen tests a constant head water tower, Figure 82, was erected to give a constant flow rate. The flow rate was measured by weighing buckets after a 1 minute, in total 12 buckets were weighed on three different days. Table 38 contains the load rate *Q* for each cylinder in N/min.

Table 38 Load Rate for Fluid Filled Specimens

TUBES	**11.8in 1 and 2**	**11.8in 3**	**4.92in All**
Rate (lb/min)	50.1	47.7	28.1
COV (%)	0.50	0.43	0.87

This test report shall not be reproduced, except in full, without the written approval of
the AEWC Advanced Structures & Composites Center.

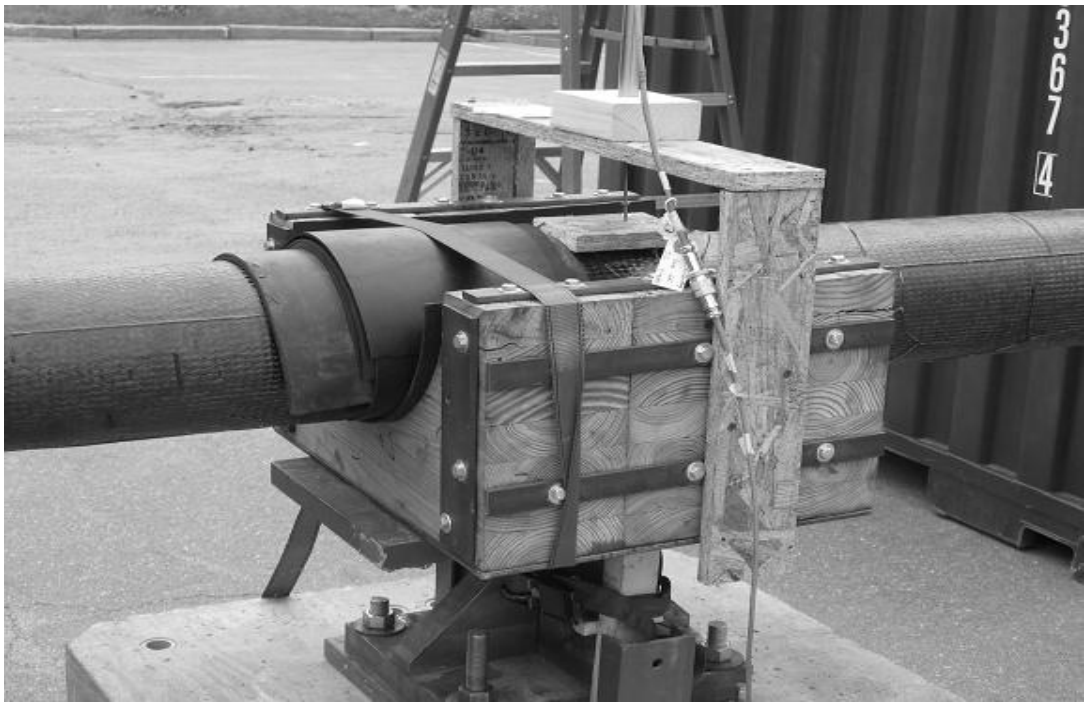

Figure 81 - Detail of Support from 6.50in Diameter Testing

This test report shall not be reproduced, except in full, without the written approval of
the AEWC Advanced Structures & Composites Center.

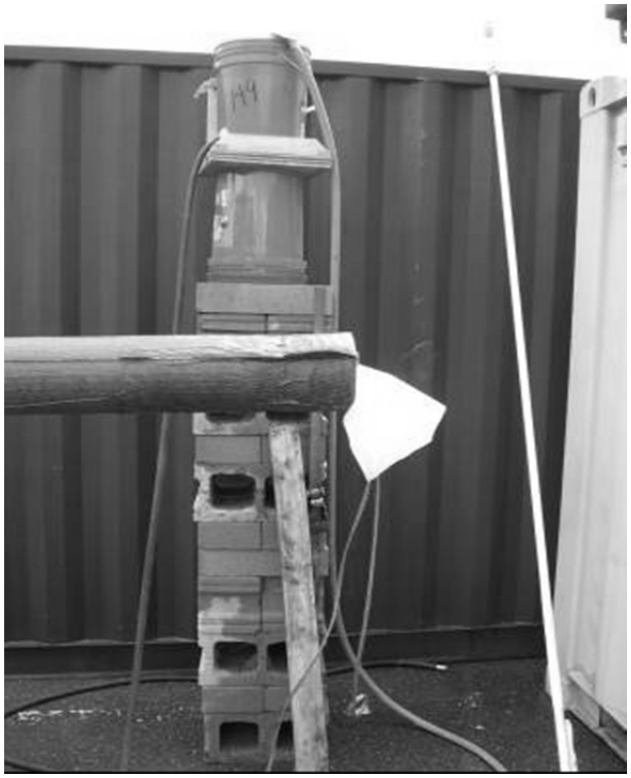

Figure 82 - Constant Head Water Tower

Instrumentation

The ovalization at a point on the tube (near midpoint) and the vertical displacement at several points along the span were measured during testing. Improvements were made to the instrumentation configuration as testing progressed. The same instrumentation was not used in every test, but for all tests the string potentiometer (string pot) configuration was similar, and 8 string pots were used. Four string pots were positioned at mid span to triangulate horizontal and vertical displacement. The other four string pots were positioned, one apiece, at the other sixth points along the specimen and positioned vertically above the starting point of the cylinder where they were connected to wooden frames. The strings were lengthened by monofilament fishing line to allow additional space between the instrument stand and the specimen and provide a mechanical fuse between the string pot and the specimen. String pots spanned from the wooden supports to screws that were fastened into small wooden blocks glued on the specimen using cyanoacrylate (super glue) and hot glue. Cyanoacrylate provided a rigid connection that did not displace during testing; hot glue provided a rapid bond until the cyanoacrylate hardened.

This test report shall not be reproduced, except in full, without the written approval of
the AEWC Advanced Structures & Composites Center.

Two modifications were made to string pot configuration between the different test periods: the gap between the specimen and the instrument stands was increased from ~9.84in to ~25.6in to reduce the effect of non-vertical displacements on string pot displacement, and the string pots at mid span were moved to get an angle further from 90 degrees (see Figure 83) to improve calculation accuracy. The side string pot in the early configuration would produce incorrect measurements as the tube displaced past the string pot. Mid span string pots were positioned to be coplanar over the connection point so that displacement in the Z and Y direction could be calculated through trigonometry.

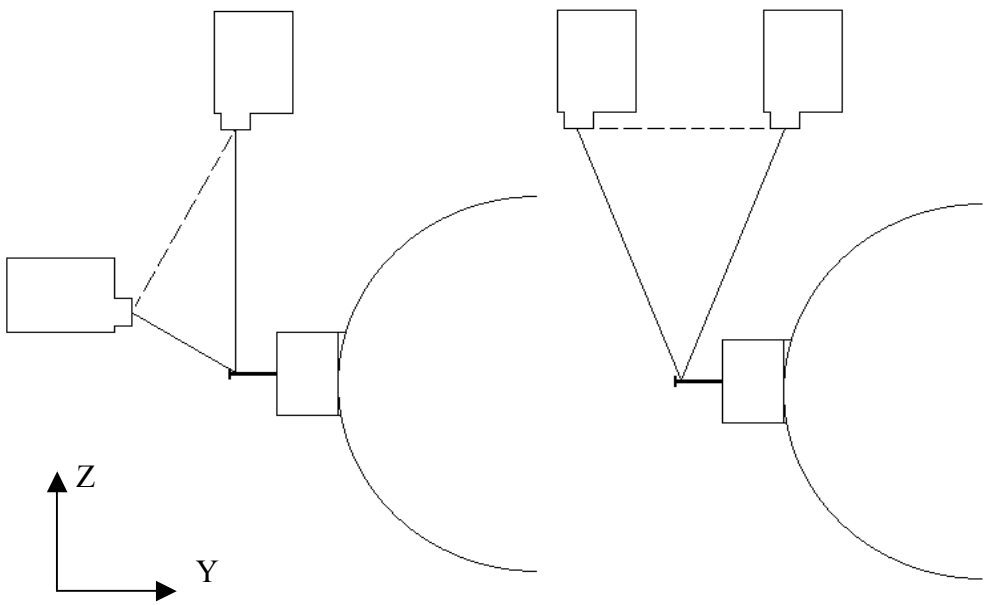

Figure 83 - Mid Span String Pot Arrangement Original and Improved

The 6.50in specimens had five additional linear variable differential transformers (LVDTs) added to measure support displacement, direct ovalization (vertical diameter loss) and mid span deflection. At supports, +/-0.984in LVDTs measured the amount the maple saddle and underlying neoprene crushed (see Figure 81), which was typically small compared to bending deflections in the span of the beam. A wooden yoke carrying a +/-0.984in LVDT was mounted to the specimen with duct tape to directly measure vertical diameter change of the specimen (Figure 84). Two long stroke (+/-5.0in) LVDTs measured vertical displacement at mid span as a check against triangulated string pot displacements and for measuring mid point deflection in point load tests (for bending stiffness *EI*).

This test report shall not be reproduced, except in full, without the written approval of
the AEWC Advanced Structures & Composites Center.

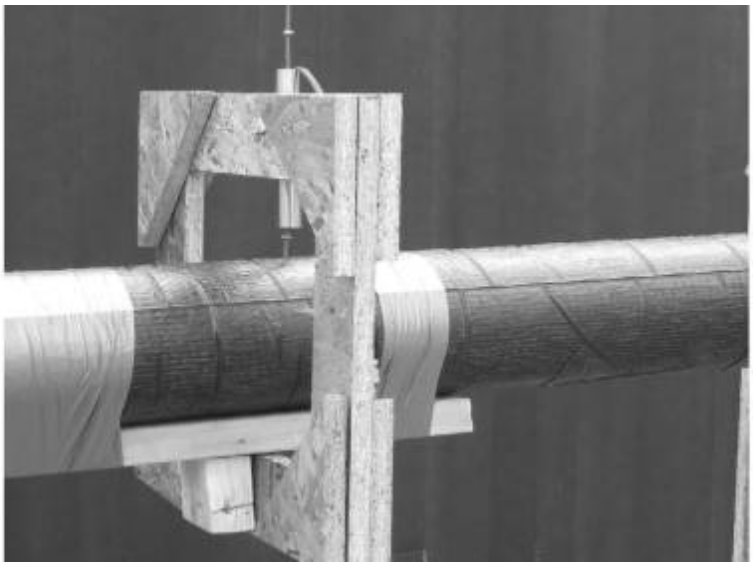

Figure 84 - LVDT Yoke for Measuring Ovalization

Results

The 11.8in diameter glass fiber specimens were loaded to failure, whereas the 6.50in diameter carbon fiber specimens were not intended to fail during testing, only ovalize. However, two carbon fiber (single carbon) specimens failed during testing. For the glass fiber specimens all three samples failed in local buckling at or near mid span (within 29.9in) and specimens G2 and G3 failed in the anticipated collapse of the compression face. Visual inspection of the tubes after failure shows that the tension face did not fracture or show signs of matrix damage even during the collapse for tube G2 and G3. Tube G1 had manufacturing defects, half of the cross section was resin poor, the other half was resin rich. The tube was arranged with the neither the center of the resin rich or resin poor sides on the compression face. Failure was asymmetric; the resin poor portion of the compression face collapsed before the resin rich portion. The resulting load redistribution caused buckling on the bottom of the tube in the resin poor portion of the face.

The carbon fiber specimens failed further from mid span with tube C1 failing outside of the middle third by ~11.8in (west) and tube 2C failing ~31.5in (east) from mid span. Both failures occurred when the specimen was nearly full and near the peak stress, as seen in later sections.

This test report shall not be reproduced, except in full, without the written approval of
the AEWC Advanced Structures & Composites Center.

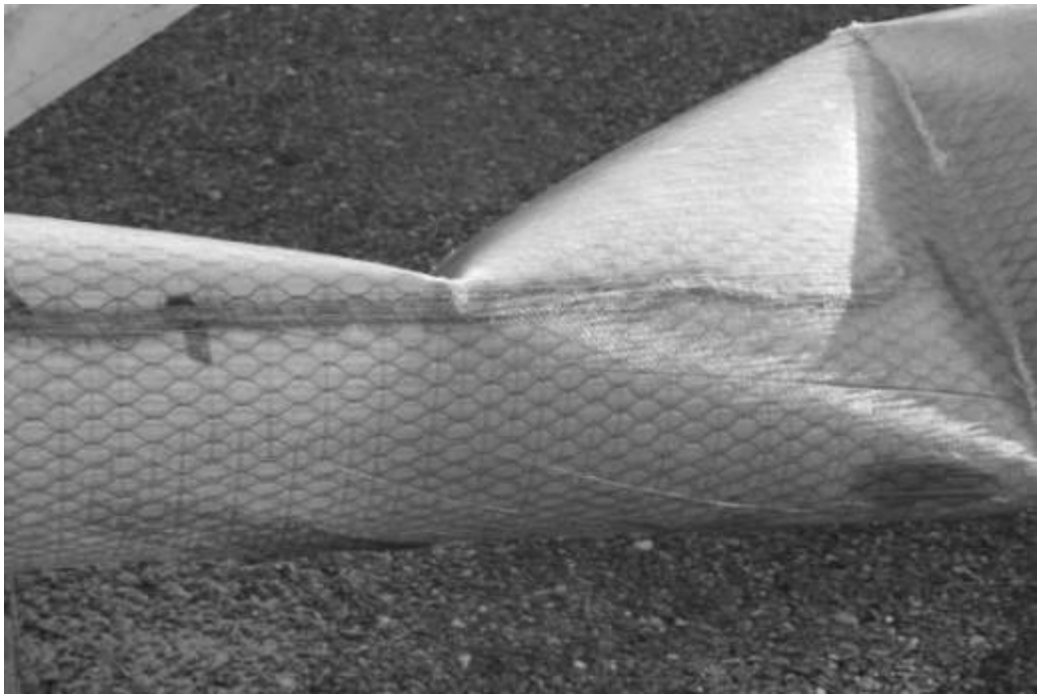

Figure 85 - Tube G1 Asymmetric Local Buckling of the Compression Face

This test report shall not be reproduced, except in full, without the written approval of
the AEWC Advanced Structures & Composites Center.

Figure 86 - Tube G3 Symmetric Local Buckling of the Compression Face

Analysis Procedure

Strain gauges were not applied to the tubes, and no direct measurement was taken of the strain within each specimen. To calculate stress in a specimen a MATLAB program was written that used the deflection and vertical radius decrease as inputs and used the flow rate from the given test to compute the fluid loads along the length based on actual and interpolated deflections and pooled fluid weight. Ponding was a significant phenomenon in these tests; often the center deflection of the 6.50in diameter specimens exceeded 6.50in during filling, making it possible for the center to be fully filled while the sides were effectively empty. In this analysis, the water was treated as a non-viscous fluid and for calculation purposes it was assumed that the water instantly flowed to an even elevation across the entirety of the specimen. The density of water was taken as 0.036lb/in^3 in all calculations.

This test report shall not be reproduced, except in full, without the written approval of
the AEWC Advanced Structures & Composites Center.

Deflection and Diameter Measurement

During the test, deflection was measured at five evenly spaced 5.0ft intervals along the length of the 30ft-span. Only gravity loads (self weight and water) were applied to the specimen during testing; it was assumed that the beam did not shift position along its length. With this assumption, the string pots only moved out-of-plane (*Y*) and vertically (*Z*). For string pots away from mid span all deflection was assumed to come from vertical displacement. This assumption was truer for the later specimens with longer initial string extensions (a 9.84in string with an extreme 1.97in out of plane motion gives a 0.20in error in deflection, a 25.6in string with the same 1.97in out of plane motion gives a 0.079in error). The endpoints were fixed against vertical deflection and the supports were rigid (there was a .118in piece of neoprene in the saddle support but its change in thickness was considered negligible for testing 11.8in specimens, and the total thickness change at the support was found to be less than or equal to 0.034in when measured during subsequent testing). Data for a specific time was not taken from a single time step but was taken as the average of (11) 1-second intervals immediately surrounding the time to account for instrumentation fluctuation.

Instead of using a single string pot at mid span, 4 string pots were used at mid span to capture the horizontal radius growth of the cross section. Two string pots connected to each side of the tube measured the change in length of two legs of a triangle; the third leg is the fixed distance between gauges. An out of plane (*Y*) and vertical (*Z*) deflection at each side of mid span was calculated. The difference in x-position on each side of the tube was taken as the horizontal radius growth. This measurement technique was sensitive to error and ultimately results of the horizontal radius measurement were deemed inaccurate due to the possibility of tube torsion, irregular cross sectional warping, and longitudinal shift that, while small, obfuscated the small horizontal radius change. Attempts to improve the method such as moving the gauges to a better initial angle near 60 degrees instead of an angle near 90 degrees did not substantially improve the quality of the data. A more successful technique was direct measurement of the vertical radius change by an LVDT on a yoke. This method produced more accurate results that, due to instrumentation faults, were not available on every 6.50in diameter test (including the failure of Specimen 1). The yoke was not used on any 11.8in diameter tests.

The MATLAB function interp1 was used with a cubic-spline shape to interpolate deflections using measured values. Figure 87 is a sample graph of the interpolated shape at 120second time intervals (and immediately before failure). The measured points are at 0ft, 5.0ft, 10.0ft, 15.0ft, 20.0ft, 25.0ft, and 30.0ft.

This test report shall not be reproduced, except in full, without the written approval of
the AEWC Advanced Structures & Composites Center.

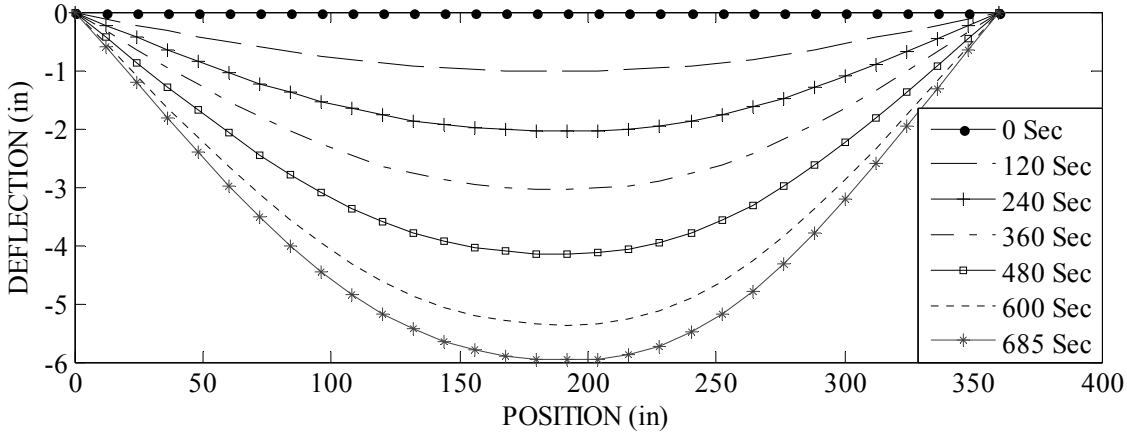

Figure 87 - Tube 2 Deflection versus Length at 120 Second Intervals

Ovalization

Determining cross sectional distortion at failure and during the test as a function of bending stress were the main reasons for fluid fill testing. Also of interest was the significance of cross sectional shape change on the section modulus and allowable stress (see modeling of compression testing). Under bending stresses the cross sectional shape of a tube or arch will change based on the curvature and the bending stress; this phenomenon is known as ovalization. The mechanism for ovalization is the bending stress acting through the curvature of the beam, as seen in Figure 88 (Tatting, 1998).

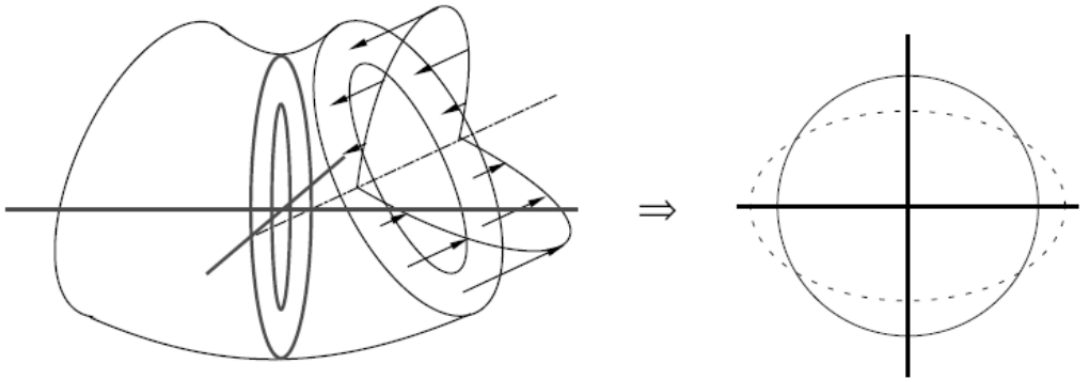

Figure 88 - Bending Stress Acting Through Deformed Tube from Tatting, 1998

Brazier (1927) was an early researcher to observe and calculate ovalization. Simplifications were used in his formulation, and all terms above second order were

This test report shall not be reproduced, except in full, without the written approval of
the AEWC Advanced Structures & Composites Center.

excluded, i.e. the change in shape was only considered once while calculating stress, it was not recalculated to account for higher stress of the deformed shape. However, later research has shown that including the next higher order term will give a less correct answer, and only a full numerical computer analysis gives a better answer than Brazier's original hand calculations (Calladine, 1983).

Brazier derived an equation that relates bending curvature to both radius change w and angular position change s, where κ is curvature; v is Poisson's ratio (Brazier assumed an orthotropic material with the same Poisson's ratio in each direction); t is shell thickness; r is shell radius; and θ is angle (counter clockwise with 0 at the vertical axis). The vertical axis loss is calculated when $\theta = 0$.

$$w = \frac{\kappa^2 r^5}{t^2}\left(1 - v^2\right)\cos(2\theta) + \kappa v r^2 \cos(\theta)$$ Equation 24

$$s = \frac{\kappa^2 r^5}{2t^2}\left(1 - v^2\right)\sin(2\theta)$$ Equation 25

In Figure 89, the Brazier shape with a 22% loss in vertical radius, which is Brazier's radius change at collapse, is plotted with an equivalent vertical radius ellipse and an undeformed circle. Brazier's shape and the ellipse are clearly very similar, and the ellipse will be used for all subsequent calculations due to the relatively simple formulae for perimeter, partial area, and section modulus of an ellipse.

This test report shall not be reproduced, except in full, without the written approval of
the AEWC Advanced Structures & Composites Center.

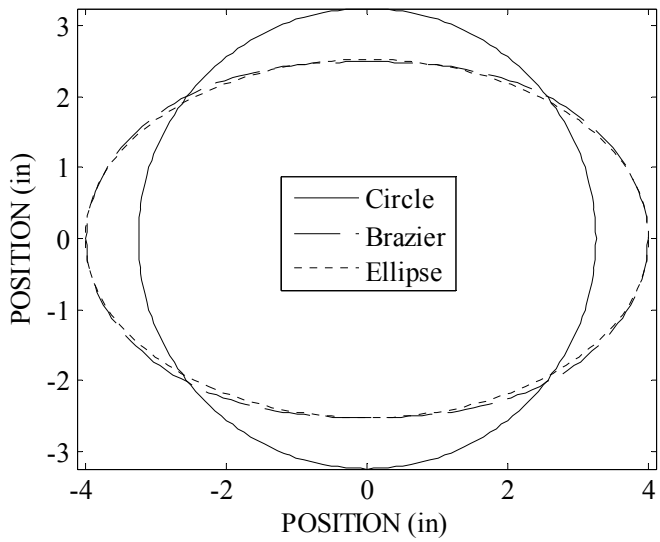

Figure 89 - Comparison of Cross Sectional Shapes

A second observation of Brazier, confirmed by later research (Tatting 1998), was that his theory predicts a theoretical ovalization limit with 22% loss of vertical radius, but local buckling can occur sooner depending on geometry and stiffness. The 22% loss in vertical radius is known as the 'collapse ovalization' and it corresponds to the point where the moment is non recoverable and increased curvature corresponds to a loss in moment capacity because of the diminishing cross sectional properties. Experimental tubes are prone to failing before this point in a lobed failure, where the cross section develops sinusoidal irregularities – as shown in the ABAQUS buckling models (see Modeling Buckling for a Hollow Cylinder). Tubes that are slender or stiffer in the longitudinal direction than the radial direction, or contain material defects, are more likely to fail prior to reaching the 'full' capacity (Tatting, 1998). Both pure compression and compressive bending stresses can produce local compressive buckling of a face on the cylinder, so the failure mode and compressive stresses at failure are assumed to be similar (Siede and Wiengarten, 1961, Tatting, 1998).

A more recent model accounts for orthotropic properties and composite laminate stacking sequence (Tatting, 1998), but this model assumes a symmetric laminate so it does not exactly satisfy the properties of the experimental specimens. Tatting based his analytical model on Brazier's model, following all assumptions used originally by Brazier. As a result, the cross section shape change predict by Tatting is identical to Brazier's, except it occurs at different stresses. Unlike the Brazier equation, the equation developed by Tatting also includes a collapse parameter dependent on a classical buckling model

This test report shall not be reproduced, except in full, without the written approval of
the AEWC Advanced Structures & Composites Center.

(Donnell, 1935) and elastic shell theory (Sanders, 1950), allowing the cylinder to fail before the Brazier predicted ovalization maximum of 22%.

The collapse load for this material was established in Compression of Hollow FRP; the experimental collapse loads P_{cr} will be used as well as a predicted collapse load (per shell length) given by Equation 26 for all carbon specimens. No experimental compression load is available for glass only specimens. Internal pressure was low for the tube fill test; it is omitted from the following equations. Also required to calculate cross section loss is a collapse parameter χ, Equation 27, dependent on shell stiffness. This parameter allows for variation due to stacking sequence by using E_x, E_θ, and D_{11} and D_{22} from the composite compliance matrix. Normalized curvature c, Equation 28, is curvature scaled relative to the local buckling collapse load for a cylindrical shell; experimental values will be used in addition to model predictions. The collapse curvature c_{lt}, Equation 29, depends on the collapse parameter. Radius loss w, Equation 30, depends on the previously defined parameters.

$$P_{cr} = \frac{\sqrt{D_{11}E_\theta t}}{r} \qquad \text{Equation 26}$$

$$\chi = \sqrt{\frac{D_{11}E_\theta}{D_{22}E_x}} \qquad \text{Equation 27}$$

$$c = \frac{E_x t r \kappa}{P_{cr}} \qquad \text{Equation 28}$$

$$c_{ltt} = \frac{1}{\chi}\sqrt{\frac{2}{3}} \qquad \text{Equation 29}$$

$$w = \frac{\chi^2 c^2}{12} \qquad \text{Equation 30}$$

A common assumption for treating ovalization phenomenon is a constant shell perimeter (Brazier, 1927, Kedward, 1978, Calladine, 1983, Tatting, 1998). The radial elastic modulus is several orders of magnitude higher than the transverse stiffness (i.e. only a small force is required in the direction of the cross-sectional radius to start flattening the hollow tube) for thin-walled sections (Brazier 1927, Tatting 1998). Also assumed was that all tubes were linear elastic until buckling. FRP composites typically exhibit linear

This test report shall not be reproduced, except in full, without the written approval of
the AEWC Advanced Structures & Composites Center.

elastic behavior; the fibers are linear elastic until failure, fail before the polymer matrix, and have an elastic modulus greater than an order of magnitude higher than the matrix.

Table 39 contains the direct measured percentage ultimate vertical radius change and the indirect calculated vertical radius change based on the measured horizontal radius change found with triangulated string pots for all specimens tested. The values are given in bold type for specimens that failed during the test to differentiate from the specimens that were only tested to deflection.

Several specimens did not have measured radius changes either because of instrumentation failure or faulty measurement, most notably test C1-top, where because of a faulty LVDT and improper string pot configuration no accurate radius measurements were taken. Measured horizontal radius increase (from string pot triangulation) was typically much higher than the directly measured vertical radius decrease; this is inconsistent with the ellipse or Brazier shape change that suggests both axes should deform nearly equally. While there may have been differential shape change, it is more likely that one or both measurement systems had inherent flaws. The vertical radius change should have been more accurate for small radius changes as it was directly measured with the yoke on the carbon fiber tubes. In the case of large radius changes, which was more typical the glass tubes G1 – G3, the error in measurement becomes smaller relative to the actual quantity being measured and the horizontal radius change is more likely to be accurate.

This test report shall not be reproduced, except in full, without the written approval of
the AEWC Advanced Structures & Composites Center.

Table 39 Maximum Percent Change in Vertical Radius from Bending Tests

Specimen	Indirect Radius	Direct Radius
G1	**25**	-
G2	**21.1**	-
G3	**20.2**	-
C1t	-	-
C2t	**6.6**	**3.29**
C3t	5.43	2.38
C3s	6.46	2.15
C4t	5.63	-
C4s	-	2.01
C5t	4.62	0.5
C5s	2.61	0.43
C6t	3.21	0.185
C6s	1.37	-

Perimeter

Measurements gave a single radial change, either vertical or horizontal. The second radius was calculated assuming a constant perimeter. Equation 31 shows the Ramanujan approximation for the perimeter of an ellipse (Sykora, 2010). This approximation is less computationally intensive than an integral and matches the Taylor series of the integral for the first 9 terms (Sykora, 2010). Known quantities A (known radius) and p (perimeter) allow for B – the other radius – to be found using Newton's method, an iterative approach where the difference between guesses is linear; the initial guess for B was the circular radius.

This test report shall not be reproduced, except in full, without the written approval of
the AEWC Advanced Structures & Composites Center.

$$p = \pi\left(r_A + r_B\right)\left[1 + \frac{3\left(\frac{\left(r_A - r_B\right)^2}{\left(r_A + r_B\right)^2}\right)}{10 + \sqrt{4 - 3\left(\frac{\left(r_A - r_B\right)^2}{\left(r_A + r_B\right)^2}\right)}}\right] \qquad \text{Equation 31}$$

Fluid Cross-Sectional Area

The cross sectional area of the fluid was calculated at each node in the tube for a specified time in the fill. The three additional assumptions to the interpolated displaced shape used in calculating the cross sectional area were: fluid settles to a level height (shown in Figure 90), flow rate was constant (volume of fluid depended on time), and a simplified method of determining the ovalization at discrete points could be used. The first two assumptions have already been discussed. The middle third of the tube has a moment within 20% of the maximum moment; therefore it is likely that for a uniform tube the ovalization is close to uniform over this region. Over the end thirds the moment diminishes rapidly to 0 at the pinned supports, and at the supports the cross sectional shape was fixed by pressurized plugs meaning that there is no ovalization at the support. An assumption was made that the radius change varies linearly from a circle at the supports to the radius change at the third point.

Figure 90 - Deflected Tube with Varying Water Height, Section in Figure 91

Because of uncertainty in ovalization measurements and calculations three cross sectional shapes were considered: a circle (original shape), the ellipse based on vertical radius change (direct measurement) or an ellipse based on horizontal radius change (triangulation). For the ellipses considered, there is small change in the area, but the partial filled area can have a larger change because of the shorter cross sectional height of an ellipse, as shown in Figure 91.

This test report shall not be reproduced, except in full, without the written approval of
the AEWC Advanced Structures & Composites Center.

Figure 91 - Cross Section of Partially Filled Tube

The area was found at each node by solving the integral in Equation 32 for the partial area of an ellipse, A_p, where h is the depth, r is the circular radius, x is the variable of integration, and all other variables are the same as calculating the perimeter of an ellipse.

$$A_p = 2\frac{r_A}{r_B}\int_0^h \sqrt{2r_B x - x^2}\, d(x) \qquad \text{Equation 32}$$

When using the circular cross section assumption the two radii are equal and the equation simplifies to Equation 33, which can be represented without an integral.

$$A_p = 2\int_0^h \sqrt{2rx - x^2}\, d(x) = \frac{r^2}{2}\left[\pi + 2\arcsin\left(\frac{h}{r} - 1\right) + \left(\frac{h}{r} - 1\right)\sqrt{\frac{h^2}{r^2} - \frac{2h}{r}}\right] \qquad \text{Equation 33}$$

Conservation of Volume

At each node, tributary volume V_i, Equation 34, was calculated using partial filled area and tributary length L_i.

$$V_i = A_{p_i} L_i \qquad \text{Equation 34}$$

Density of the water does not appreciably change throughout the experiment and a constant delivery of water is assumed; there must be a constant increase in volume. The total fluid volume V_t, Equation 35, was known from the fluid load rate Q, the density of water ρ and the time duration t_{fill}.

This test report shall not be reproduced, except in full, without the written approval of the AEWC Advanced Structures & Composites Center.

$$V_t = \frac{Q}{\rho} t_{fill}$$ Equation 35

Using Newton's method, the depth of fluid in the tube D was manipulated until the sum of nodal volumes equaled the total volume V_t. To begin the iterative process for fluid depth an initial guess was needed to calculate nodal volumes, mid span deflection was chosen, meaning that the initial guess made the fluid height level with the elevation of the supports. A numerical derivative for the volume with respect to depth $d(V_i)/d(D)$, needed for Newton's method, was calculated using forward difference method and a small change in depth. Equation 36
shows the calculation of the updated depth D performed at each Newton iteration.

$$D = D - \frac{V_t - \sum V_i}{\frac{d(V_i)}{d(D)}}$$ Equation 36

The fluid area was recalculated for the updated depth. This process was iterated until the volume difference for the entire tube between the total volume and the summed nodal volumes was less than .000061in^3.

Point Forces

The force applied to the tube by water loading was treated a series of point loads applied at the nodes. Figure 92 shows a beam with the non-uniform distributed load of water weight divided into point loads. The magnitude of each nodal force was equal to the density of water times the volume of water in the space tributary, using the optimized volume from Newton's method at each node. The density of water was taken as 0.036lb/in^3.

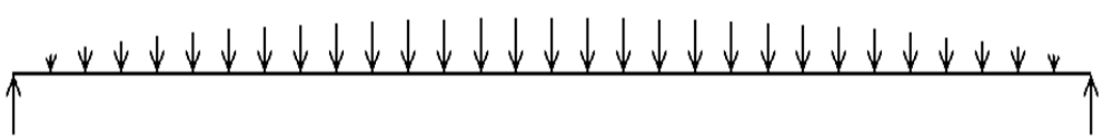

Figure 92 - Beam with Applied Fluid Load

This test report shall not be reproduced, except in full, without the written approval of
the AEWC Advanced Structures & Composites Center.

Bending Stresses and Displacements

The right vertical reaction, R_{right}, was calculated by summing moments about the reaction assuming a simply-supported beam. In Equation 37, P is a point force caused by water weight; l is the distance from the left support to the point force; n is the number of point forces; and L is the span (distance between centerline supports).

$$R_{right} = \sum_{i}^{1:n} \frac{P_i l_i}{L} \qquad \text{Equation 37}$$

After generating the left reaction, the internal moment at each node was calculated by summing the moments caused by all nodal forces between the left support and the node of interest at each node. In Equation 38, the addition sign implies that standard engineering sign conventions are used and the reaction will always points upward and the point forces point downward (gravity).

$$M_k = R_{left} l_k + \sum_{i}^{1:k} P_i \left(l_k - l_i \right) \qquad \text{Equation 38}$$

The maximum bending stress at a point (F_b) is the internal moment divided by the section modulus. The section modulus for a hollow ellipse, Equation 39, is the difference of the moment of inertia of the solid (outer) ellipse and the hollow (inner) ellipse divided by the radius of the solid ellipse (total centroidal height).

$$S_x = \pi \left(\frac{r_A r_B^{\,3} - \left(r_A - t \right)\left(r_B - t \right)^3}{4 r_B} \right) \qquad \text{Equation 39}$$

Table 40 contains the maximum computed stress in each bending test based on the three assumed cross sectional shapes. All specimens that failed during testing are listed in bold type. For specimens that did not fail, stress was limited by water capacity, and tests were stopped once water came out of the fill hole. These specimens were tested with their arbitrarily named 'top' side up, and then were rotated 90 degrees and tested again on their 'side', moving defects and getting more ovalization data from the same number of specimens.

Specimens G1-G3 (the longitudinal glass fiber specimens, which were tested first) have a large difference in stress from the circular cross section to the ellipse cross section. At failure, the elliptical cross section was measured to be near Brazier's collapse ovalization (22%), and this large shape change has a 4.8% reduction in section modulus versus a circle (there is a .4% loss in section modulus for a 6% loss in vertical radius). The glass

This test report shall not be reproduced, except in full, without the written approval of
the AEWC Advanced Structures & Composites Center.

fiber tubes failed at around 50% fluid capacity; there was a large difference between the amount of water in a partially filled flat ellipse and a partially filled circle with the same hydraulic elevation. Carbon fiber tubes exhibit a similar stress for both the circle and ellipse cross-sections because they experienced less ovalization. The difference in section modulus was less than 1% from the initial circle for all carbon fiber tubes and the tubes failed or finished filling when the center was full.

Brazier's equation for radius change is based on an isotropic material – uniform elastic modulus in all directions – not an irregular material such as a multilayer composite shell. When the shell is modeled as an orthotropic material using Classical Lamination Theory (CLT) there can be a large discrepancy between the longitudinal elastic modulus and the radial elastic modulus (transverse in CLT). The all glass fiber tubes (G1-G3) had a radial modulus nearly double the transverse modulus, while the single carbon fiber tube had the opposite relationship, a longitudinal modulus more than double the transverse modulus. Specimens that were relatively stiff in the radial direction were more likely to oval severely before buckling, sometimes reaching the maximum collapse ovalization and the Brazier collapse moment.

Table 40 Maximum Bending Stress in Ksi

Specimen	Circle	Ellipse - Vertical	Ellipse - Horizontal
G1	5.11	-	6.14
G2	5.42	-	6.74
G3	5.57	-	6.87
C1-top	9.27	-	-
C2-top	8.46	8.66	8.88
C3-top	10.4	10.6	10.7
C3-side	10.4	10.5	10.8
C4-top	10.3	-	10.6
C4-side	10.1	10.3	-
C5-top	7.05	7.05	7.14
C5-side	6.95	6.96	7.12
C6-top	6.74	6.76	6.92
C6-side	4.28	-	4.32

This test report shall not be reproduced, except in full, without the written approval of
the AEWC Advanced Structures & Composites Center.

The described analysis method for generating a series of point loads from deflected shape and fluid ponding was not a usual method for analyzing a beam or running a laboratory test. To check the accuracy of the assumptions and the measured deflections, the center deflection for each tube was calculated using finite element beam code and the calculated load based on filled fluid volume. A model was constructed with two-noded Euler Bernoulli beam elements. Nodes were distributed at the same locations as water testing analysis, cross section shell area A and moment of inertia I were based on the deformed cross section (different deflections are generated based on model assumptions) and varied along the length of the beam, and the elastic modulus was based on the experimental bending modulus from sand bag tests in Table 37. The beam was given simple supports; the left support was a pin, the right support was a roller.

Three cross section shapes: circle, ellipse based on measured vertical deflection, and ellipse based on measured horizontal deflection, give different deflections. The ellipse prediction based on horizontal measurements generates the largest deflection prediction because it had the smallest moment of inertia. As seen from the results, actual mid span deflections were close to model predictions, frequently having less than 10% difference. The vertical measured deflection gave the best prediction for mid span deflection, the model over predicts deflection in five of nine tests, showing an almost even number of times above and below the predicted value. This assumption also had two trials with less than 1% difference between measured and predicted deflection and an additional three trials with less than 5% difference between measured and predicted deflection. Figure 93 shows the measured and predicted mid span deflection, assuming the vertical radius measured shape change, for the duration of the test C4-side. In this plot, the measured and predicted deflections remain close except for a single point where the vertical deflection jumps.

This test report shall not be reproduced, except in full, without the written approval of
the AEWC Advanced Structures & Composites Center.

Table 41 Actual and Predicted Deflection in inches and % Difference

Test	Actual	Circle	% (A-C)	Vertical	% (A-V)	Horizontal	% (A-H)
C1-top	6.06	5.83	-4.12	-	-	-	-
C2-top	6.26	5.24	-16.5	140	-12.0	148	-6.88
C3-top	6.26	6.73	8.00	177	11.5	186	17.0
C3-side	6.14	6.73	9.59	178	13.7	188	20.3
C4-top	6.97	6.61	-4.75	169	-4.46	183	3.45
C4-side	6.73	6.46	-4.01	170	-0.742	-	-
C5-top	6.46	6.38	-0.930	162	-0.930	168	2.48
C5-side	6.10	6.26	2.45	161	3.27	170	9.15
C6-top	3.06	2.98	-2.61	75.9	-2.29	79.8	2.61
C6-side	1.64	1.81	10.4	46.0	10.4	47.0	12.8

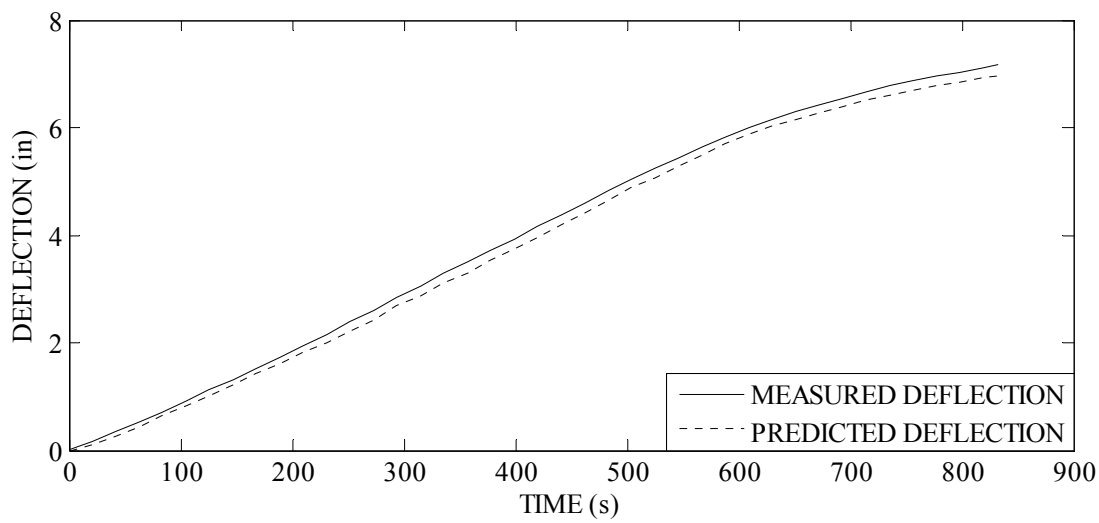

Figure 93 - Comparison of Measured and Predicted Deflection, C4-top

Later experimental tests showed that tubes C3 and C4 were slightly stronger than tubes C1 and C2, but an additional factor that may have influenced early failure was thermal

This test report shall not be reproduced, except in full, without the written approval of
the AEWC Advanced Structures & Composites Center.

gradient. Tubes C1 and C2 were both tested on sunny days while tubes C3 and C4 were both tested on overcast days. Approximately 10 minutes after the failure of tube C2 thermal readings were taken of the water inside the tube as well as the shell temperature in areas that were fully filled, partially filled, and completely empty. Exposed to direct sunlight, the black, insulating carbon fiber shell absorbed a significant amount of heat from the sun and the 30 degree temperature shift from the area cooled by the water to the top fibers exposed to direct sunlight may have contributed to cross sectional distortion influencing a lower failure stress.

Table 42. Temperature of Tube C2 After Failure, in Degrees Celsius

Air	Water	Mid Span Carbon	Sixth Point Carbon	End Carbon
23	12	28	43	52

Stress Versus Ovalization

Ovalization is a function of bending stress and curvature; in a straight linear elastic beam curvature and bending stress are directly related, making ovalization a function of bending stress. As bending stress increases in the specimen the ovalization increases; this much is consistent in every test. Two methods of measuring ovalization were used: measuring the horizontal radius growth with four string pots and triangulating to horizontal and vertical displacements and measuring the vertical radius contraction with an LVDT mounted on a yoke surrounding the tube. The glass fiber tubes G1-G3 only used horizontal radius measurement equipment, not a direct measurement of the vertical radius. Ovalization at failure closely related to the Brazier ovalization prediction at failure, but shape of the radius change versus load plots were nearly linear while the Brazier prediction indicated a sharp radius change increase at the end of the test. A high initial deflection and a nearly linear response are hallmarks of the horizontal measurement technique (Figure 94, Figure 96), a shape contrary to both predictions which indicates faster radius change as the bending stress becomes higher. In all stress versus ovalization plots, radius change refers to the vertical radius change, either directly measured or calculated from the measured horizontal radius change, and the stress was calculated using the deformed shape based on the radius change being displayed. All laminates except double carbon have the Tatting predictions extended to the collapse moment.

This test report shall not be reproduced, except in full, without the written approval of
the AEWC Advanced Structures & Composites Center.

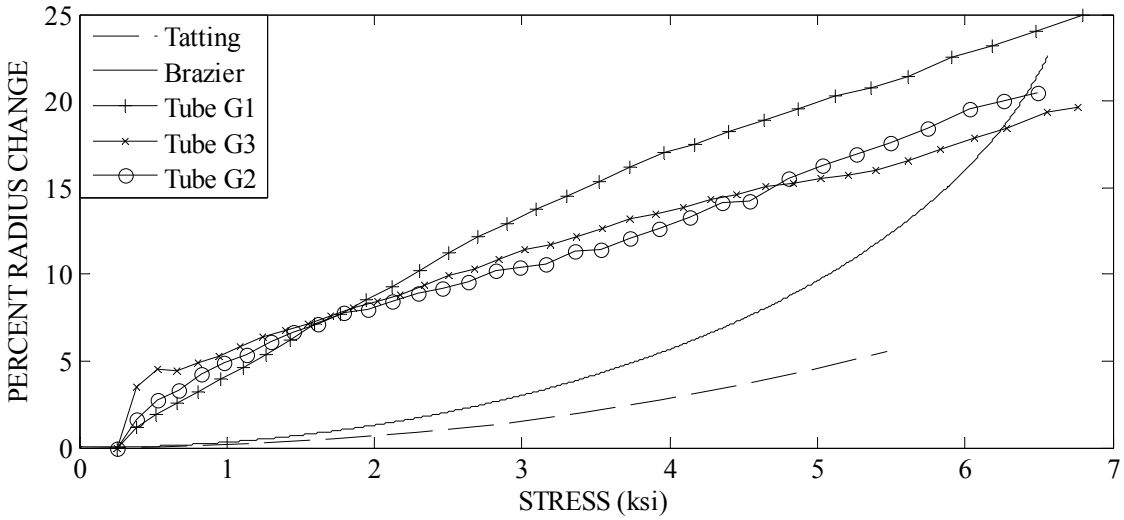

Figure 94 - Radius Change vs Stress, Glass Tubes, Horizontal Radius

Single layer carbon specimens showed a reasonable correlation between Tatting ovalization prediction and the actual ovalization from vertical measurements (Figure 95). Tube C2 ovals faster than the other tubes, but this tube failed near the LVDT measuring vertical deflection, so if a local curvature or radius defect caused a stress concentration, additional ovalization occurred in this vicinity. The horizontal measurements for all of the carbon fiber tubes are similar to the glass fiber measurements; the entire response shape is different from the shape of the Tatting prediction and the initial response is steeper (Figure 96, Figure 97, andFigure 98). Either the horizontal measurements are correct, and the tube changes shape in a very different way than thought, or the horizontal measurements are being skewed by a poor assumption. A possibility that explains the difference is longitudinal motion. Water is filled from a side, not at the center, and that side will have a higher weight of water before it distributes, causing unbalanced fluid height along the length, and potentially lateral motion in the loose lateral restraints. Results show this behavior; specimens have slower ovalization later in the test when ovalization rate should be increasing, but weight should be more evenly distributed reducing lateral translation.

This test report shall not be reproduced, except in full, without the written approval of
the AEWC Advanced Structures & Composites Center.

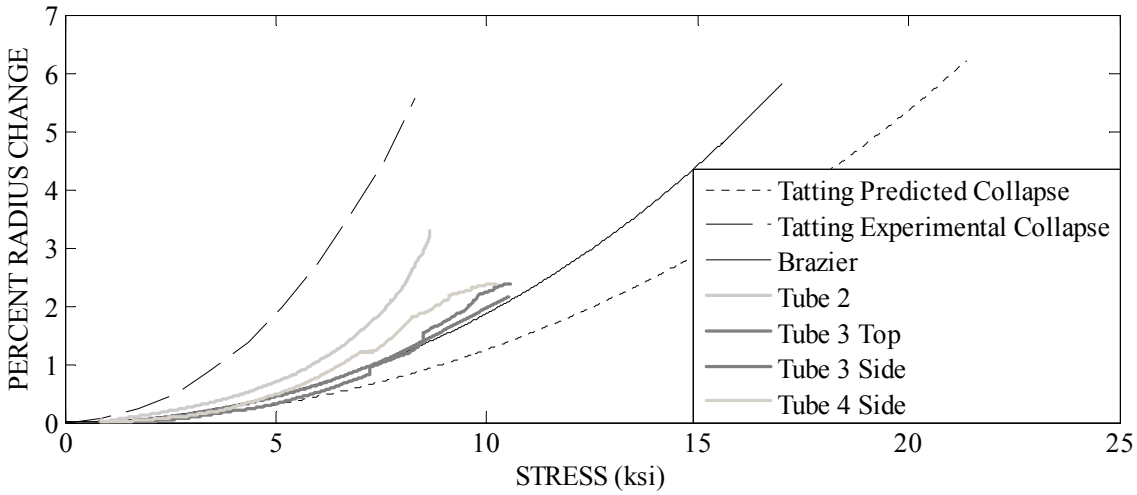

Figure 95 - Radius Change vs Stress, Single Carbon Tubes, Vertical Radius

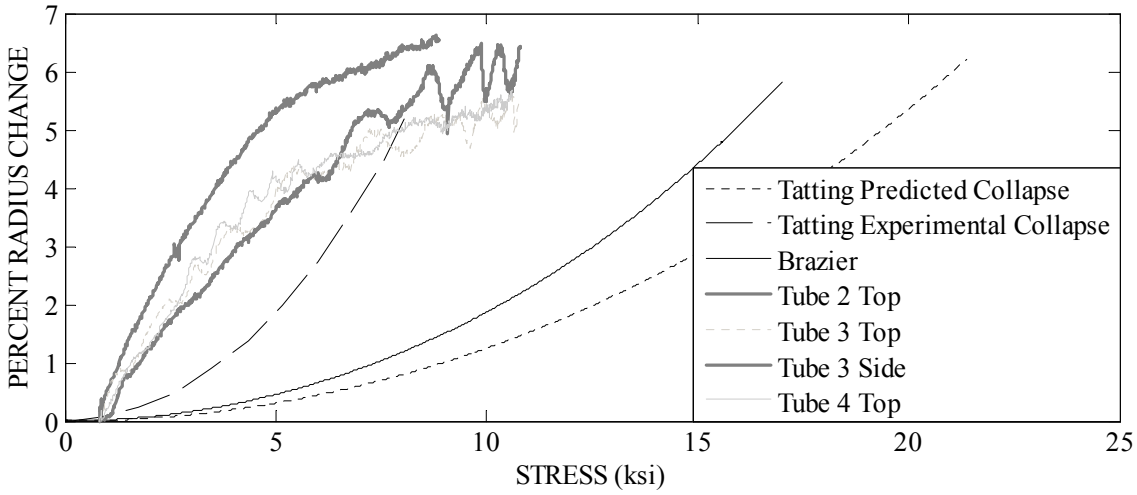

Figure 96 - Radius Change vs Stress, Single Carbon Tubes, Horizontal Radius

This test report shall not be reproduced, except in full, without the written approval of
the AEWC Advanced Structures & Composites Center.

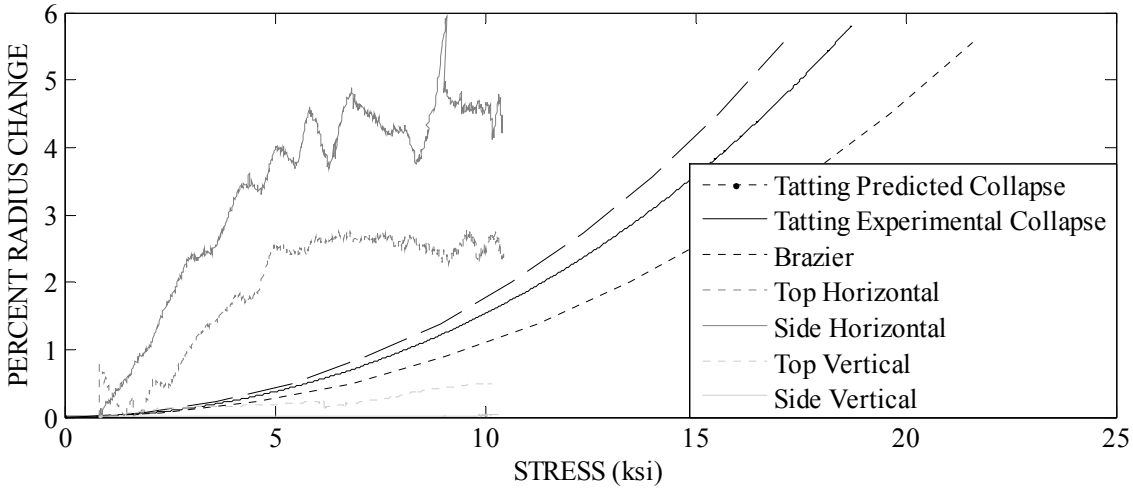

Figure 97 - Radius Change vs Stress, Bleeder Carbon Tube

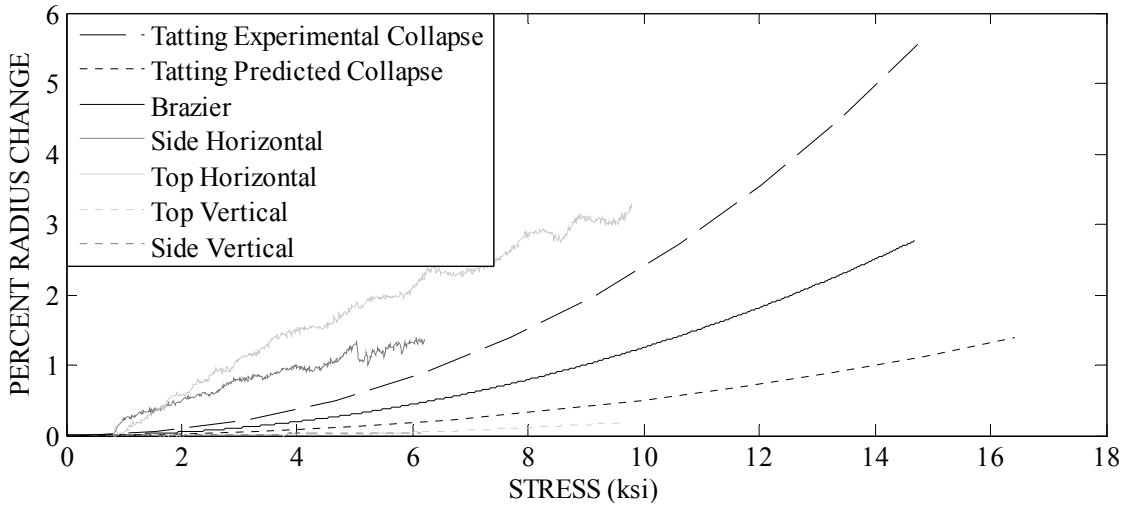

Figure 98 - Radius Change vs Stress, Double Carbon Tube

In all cases except the double carbon tube, the Brazier ovalization prediction appeared closer to experimental data than the more sophisticated Tatting prediction.

Conclusions

Bending tests were conducted on long cylinders to assess importance of ovalization, or Brazier's effect, on the bending stress in a tube. Glass fiber structural tubes showed a

This test report shall not be reproduced, except in full, without the written approval of
the AEWC Advanced Structures & Composites Center.

large change in radius that caused a noticeable reduction in section modulus; measurement indicated ~20% gain in horizontal radius before failure, and a loss of over 4% of the section modulus. The change in radius closely matched Brazier's theoretical collapse ovalization and the bending stress also corresponded closely to Brazier's ultimate moment. The amount of ovalization was likely smaller than the measurement and influenced by poor results that exaggerated early ovalization results.

Carbon fiber tubes did not respond in the same manner. Two of the four single-layer carbon fiber tubes failed during testing; both failures occurred well below the Brazier predicted collapse ovalization or moment, regardless of measurement technique. However, subsequent compression tests of short tubes, Compression of Hollow FRP, showed that the computed ~8.70ksi failure stress is not unreasonable for this material in this geometric configuration. Single carbon, short tubular compression specimens failed at an average of 11.6ksi, but individual specimen capacities varied from 8.56ksi – 17.0ksi. The lower bound of experimental compression tests corresponds to the calculated buckling stress for the bending specimen. As carbon fiber is the preferred material for longitudinal structural reinforcing, the results of these tests indicate that ovalization during filling may not be an important effect to account for when designing a beam or arch.

Ovalization cannot be used as failure criteria because there is not an ovalization that relates directly to failure; every geometry and fiber lay-up is going to have a different response. The small magnitude of the ovalization at failure for the carbon specimens (3% loss in vertical radius) is not easily seen by the human eye and is difficult to measure during a test – especially as the cross section translates and sways during a ten-minute fill. Failure will occur below the maximum ovalization, before the theoretical collapse moment, because the local buckling stress was controlled by material defects and laminate asymmetry.

Future Work

It is unlikely that these tests will be repeated as detailed here. Many improvements to the testing procedure were made between initial testing and the second round of testing. The first testing measured radius change only through string pot triangulation at mid span; after reviewing results this method was determined to be inaccurate and prone to consistent error. Initial testing had no support displacement measurement, no direct vertical radius change measurement, short string pots that were more sensitive to out of plane motion, and a water quantity that assumes tap water pressure remains constant. Yokes were not used in initial testing to prevent damage to instrumentation from the collapse of the specimen. In subsequent testing, no LVDTs were damaged by the falling tube. Later testing corrected many of these problems. LVDTs at the support measured support crushing and detected up to 0.079in of settlement in the maple saddle and the

This test report shall not be reproduced, except in full, without the written approval of
the AEWC Advanced Structures & Composites Center.

neoprene layer supporting the tube. A single yoke with an LVDT measured direct vertical diameter loss; this measurement related much better to the predicted equations in both magnitude and general shape than horizontal measurements. Additional LVDTs would have been useful to verify the radius measurement. String pots with extended strings reaching over 23.6in initially reduced error from lateral and out of plane motion. A constant head water stand was used to deliver consistent fluid pressure.

Future testing should not use more instrumentation, but better apply the instrumentation. Instead of the 4 string pots at mid span, a single string pot measuring vertical change, as at the other sixth points, would improve vertical deflection measurements. The long LVDTs used at mid span, which frequently ran out of stroke during the test, could be eliminated. Two additional ovalization measurements using vertical LVDTs could give ovalization over the length of the tube instead of a single location. Another proposed change is to test multi-layer tubes (bleeder carbon and double bleeder) at a larger span length to generate higher bending stresses. All measurements show poor ovalization correlations for these tubes, but the tubes saw low stress making the expected ovalization more affected by the error in the measurement technique.

Summary

This project dealt with the refinement of analysis methods and the improvement of design tools and some materials. Significant cost savings can be achieved with this work for most projects. Improvements to the soil-structural interaction analysis allow for a methodical and established way of allowing the soil to achieve passive or active condtions in the model. A new decking product was introduced that allows for an increased spacing of arches therefore decreasing cost and potentially eliminating the concrete overlay saving time and money. Advanced modeling of unfilled tubes gives a much greater understanding of the capacity of these unfilled tubes during construction. This allows for greater reliability in their performance and increases safety and potentially decreases cost.

This test report shall not be reproduced, except in full, without the written approval of
the AEWC Advanced Structures & Composites Center.

References

Bannon, Dan. Goslin, Keenan WI-T-77 "Static and Fatigue Testing of Cylindrical Concrete Filled FRP Beams". AEWC Internal Work Instruction. AEWC Center June 26, 2008 rev Sept 2010.

Bannon, Dan. "Characterization of Concrete-Filled Fiber Reinforced Polymer (FRP) Arch Members". Master's Thesis. University of Maine. May 2009.

Baxter, John R. "FHWA Acceptance Letter B-124". Letter to Shane Weyant at Creative Pultrusions. December 9, 2003. http://safety.fhwa.dot.gov/roadway_dept /policy_guide_/road_hardware/barriers/pdf/b124.htm. Cited July 7, 2011.

Brazier, L. G. (1927). On the flexure of thin cylindrical shells and other "thin" sections. *Proceedings of the Royal Society of London. Series A, Containing Papers of a Mathematical and Physical Character,* 116(773), 104-114.

Carey, J. et. al. (2003). Longitudinal elastic model prediction of a 2-d braided fiber composite. *Journal of Reinforced Plastics and Composites*, 22, 813-831.

Chen, L. et. al. (1999). Mechanical analysis of 3-d braided composites by the multiphase element method. *Composites Science and Technology*, 59, 2383-2391.

Clapp, Joshua. William Davids. "CFRP Arch Analysis and Theory". AEWC Technical Report 11-30. University of Maine. January 31, 2011

Creative Pultrusions, Inc. "Superdeck Technical Data". Alum Bank, PA http://www.creativepultrusions.com/LitLibrary/products/superdeck/brochure.pdf. July 22, 2011.

Cox, B. N. and Dadkhah M. S. (1995). The macroscopic elasticity of 3D woven composites. *Journal of Composite Materials*, 29, 785-819.

Daniel, I. M. and Ishai, O. (2006). Engineering mechanics of composite materials, 2nd Edition. Oxford, Ny.: Oxford University Press.

Demkowicz, M. (2011). Environmental durability of hybrid braided polymer matrix composites for infrastructure applications. (Master's thesis, University of Maine, 2011 – publishing pending).

Donnell, L. H. (1934). Stability of thin-walled tubes under torsion. *NACA TR-479*.

This test report shall not be reproduced, except in full, without the written approval of the AEWC Advanced Structures & Composites Center.

Donnell, L. H. (1934). A new theory for the buckling of thin cylinders under axial compression and bending. *Transactions of the American Society of Mechanical Engineers*, 56, 795-806.

Edgren, F. and Asp, L. E. (2005). Approximate analytical constitutive model for noon-crimp fabric composites. *Composites: Part A*, 36, 173-181.

El-Chiti, F. (2005). Experimental variability of e-glass reinforced vinyl ester composites fabricated by VARTM/Scrimp. (Masters thesis, University of Maine, 2009).

El-Chiti, I. (2004). FRP-concrete arch. (Masters thesis, University of Maine, 2009).

Enduro Systems Inc. (n. d.). Tuff Span ® 8.0 Roof Deck Series 700. In *Enduro Systems Tuff Span® Building Products Guide Catalogue.* Retrieved June 2, 2011, from <http://www.endurocomposites.com/downloads/Enduro_Tuff_Span_Building_Products_Guide_Catalog.pdf>.

Faraji S, Ting JM, Crovo DS, Ernst H (2001). Nonlinear analysis of integral bridges: finite-element model. *Journal of Geotechnical and Geoenvironmental Engineering*, 127(5): 454-461.

Fuchs H. P. and Hyer M. W. (1996). The nonlinear response of short thin-walled laminated composite cylinders in bending. *Composite Structures*, 34, 309-324.

Goslin, Keenan. Neal Bridge Replacement-Structural Calculations. AEWC project 622. February 2, 2009.

Harajli, M. H. (2006). Axial stress-strain relationship for FRP confined circular and rectangular concrete columns. *Cement & Concrete Composites* 28, 938-948.

Jiang , T. & Teng, J. . (2007). Analysis-oriented stress-strain models for FRP-confined concrete. *Engineering Structures,* 29, 2968-2986.

Jones, R. M. (1975). Mechanics of composite materials. Washington DC: Hemisphere Publishing Company.

Jones, R. M. (2006). Buckling of bars plates and shells. Blacksburg Va.: Bull Ridge Publishing.

This test report shall not be reproduced, except in full, without the written approval of the AEWC Advanced Structures & Composites Center.

Kedward, K.T. (1978). Nonlinear Collapse of thin-walled composite cylinders under flexural loading. *Proceedings, 2nd International Conferece on Composite Materials,* Metal Society of AIME, Warrendale Pa., 353-365.

Lei, C. et. al. (1992). Finite element analysis of 3-d braided composites. *Advances in Engineering Software*, 14, 187-194.

Li, L. Y. (1996). Bending instability of composite tubes. *Journal of Aerospace Engineering*, 9 (2), 58-60.

Martin Marietta Composites. "DuraSpan fiber-reinforced polymer bridge deck systems". Raleigh, North Carolina. www.martinmariettacomposites.com. July 22, 2011.

Mostoller, Jeremy. "Arch Sheathing Panel: Global sizing Verification". Engineering report from Creative Pultrustions, Inc. to Advanced Infrastructure Technologies, LLC. January 20, 2011.

Nairn J. A. (1997). On the use of shear-lag methods for analysis of stress transfer in unidirectional composites. *Mechanics of Materials*, 26, 63-80.

NCHRP (1991). *Manuals for the Design of Bridge Foundations*. National Cooperative Highway Research Program Report No. 343, Transportation Research Board, Washington, DC.

Reissner, E. and Weinitschke, H. J. (1963). Finite pure bending of circular cylindrical tubes. *Quarterly Journal of Applied Mathematics,* 20, 305-319.

Richards, Dan. Phone Interview with Brad Hall regarding ZellComp decking capacity. August 8, 2011.

Resolite. Tred Safe Roof Panels Datasheet. San Diego, CA. http://www.fiberglasssheets.com/FRP/Resolite-Tred-Safe-Roof-skylight-fiberglass-roof-panels. July 22, 2011.

Saha, M., Prabhakaran, R., Waters, W. A. Jr. (2004). Compressive behavior of pultruded composite plates with circular holes. *Composite Structures*, 65, 29-36.

Sanders, J. L. (1970). Nonlinear theories for thin shells. *Quarterly Journal of Mechanics and Applied Mathematics,* 21, 25-36.

This test report shall not be reproduced, except in full, without the written approval of the AEWC Advanced Structures & Composites Center.

Seide, P. and Weingarten, V. I. (1961). On the buckling of circular cylindrical shells Under pure bending. *Journal of Applied Mechanics,* 28, 112-116.

Shen, H. S. (2008). Boundary layer theory for the buckling and postbuckling of an anisotropic laminated cylindrical shell. Part I: prediction under axial compression. *Composite Structures*, 82(3), 346-61.

Silvestri, N. (2007). Generalised beam theory to analyse the buckling behaviour of circular cylindrical shells and tubes. *Thin-Walled Structures*, 45, 185-198.

Soutis, C, and Fleck, N. A. (1990) Static compression failure of carbon fibre T800/924C composite plate with a single hole. *Journal of Composite Manufacture*, 24, 536-558.

Sykora, S. (2010). Ellipse Perimeter Approximations. *Stan's Hub,* Web, 10 Mar. 2011. <http://www.ebyte.it/library/docs/math05a/EllipsePerimeterApprox05.html>.

Tatting, B.F., Gurdal, Z. and Vasiliev, V. V. (1997). The Brazier effect for finite length composite cylinders under bending. *International Journal of Solids and Structures*, 34, 1419-1440.

Tatting, B.F. (1998). Analysis and design of variable stiffness composite cylinders. (PhD thesis, Virginia Polytechnic Institute and State University, 1998).

Ting JM and Faraji S (1998). *Force-Displacement Testing for Integral Abutment Bridges*. University of Massachusetts Transportation Center Report No. UMTC 97-13, University of Massachusetts, Amherst, MA.

Tomblin, J. (2006). Buried frp-concete arches. (Masters thesis, University of Maine, 2006).

Toutanji, H. A. (1999). Stress-strain characteristics of concrete columns externally confined with advanced fiber sheets. *ACI Materials Journal,* 96(3), 397-404.

USACoE (1994). *Design of Sheet Pile Walls*. CECW-ED Engineer Manual 1110-2-2504. Department of the Army, US Army Corps of Engineering, Washington, DC.

This test report shall not be reproduced, except in full, without the written approval of the AEWC Advanced Structures & Composites Center.

Walton, Harold. "Response of FRP Arches to Concrete Filling Loads". Master's Thesis. University of Maine. August 2011.

Weaver, P. M. (2002). Anisotropy-induced spiral buckling in compression-loaded cylindrical shells. *AIAA Journal*, 43, 2639-2645.

Wierzbiecki, T. & Sinmao, M. V. (1997). A simplified model of Brazier effect in plastic bending of cylindrical tubes. *International Journal of Pressure Vessels and Piping*, 71(1), 19-28.

Zellcomp. Fiber-reinforced composite bridge decks. Durham, NC. www.zellcomp.com. July 22, 2011.

Zeng, T. et. al. (2004). Mechanical analysis of 3d braided composites: a finite element model. *Composite Structures*, 64, 399-404.

This test report shall not be reproduced, except in full, without the written approval of the AEWC Advanced Structures & Composites Center.

APPENDIX A: – SUPPORTING CALCULATIONS

This test report shall not be reproduced, except in full, without the written approval of
the AEWC Advanced Structures & Composites Center.

Page: 1
By: JDC Date: 5/2/2011
Checked by: ____ Date: 5/2/2011

AEWC Center

5793 AEWC Building
Orono, Maine 04669
Telephone: (207) 581-2123
Fax: (207) 581-2074
www.aewc.umaine.edu

Designed By: JDC
Date: 01/20/11
Checked By:
Date:
Job Number: 906F

Project: AIT Soil-Structure Interaction
Task: Calculate Analysis Properties

References

1. Proposed decking design drawing provided by Matthew Pellerin of AIT.

Uncracked decking properties in the transverse direction (spanning arches)

AASHTO 2007 allows either uncracked or cracked sections to be considered depending on the expected situation, assume cracked

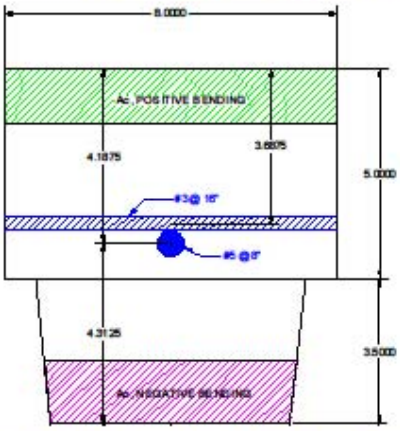

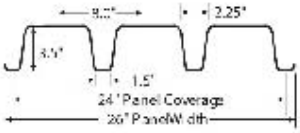

Concrete section - perpendicular to arch span (some properties from AutoCAD)

TRANSVERSE

$$Ag := \frac{21.44in^2 + 8in \cdot 5in}{8in} = 7.68 \cdot \frac{in^2}{in}$$

Concr. strength $f_c := 4350psi$ *(MDOT spec.)*

Concr. stiffness $E_c := 57000 \cdot \sqrt{f_c \cdot psi}$ $\boxed{E_c = 3759 \cdot ksi}$

Modular ratio $n_s := \frac{29000ksi}{E_c}$ $n_s = 7.71$

UNCRACKED

Ybar (top)

$$y_t := \frac{8in \cdot 5in \cdot 2.5in + 21.44in^2 \cdot 6.71in + \frac{\pi}{4} \cdot \left(\frac{5}{8}in\right)^2 \cdot (n_s - 1) \cdot 4.18in}{8in \cdot 5in + 21.44in^2 + \frac{\pi}{4} \cdot \left(\frac{5}{8}in\right)^2 \cdot n_s}$$ $y_t = 3.96 \cdot in$

C:\Documents and Settings\joshua.clapp\Desktop\Arch Decking Calcs.xmcd

This test report shall not be reproduced, except in full, without the written approval of the AEWC Advanced Structures & Composites Center.

This test report shall not be reproduced, except in full, without the written approval of
the AEWC Advanced Structures & Composites Center.

Page: 2
By: JDC Date: 5/2/2011
Checked by: ___ Date: 5/2/2011

TRANSVERSE (continued)

Moment of inertia

$$I := \frac{\frac{8in\cdot(5in)^3}{12} + 8in\cdot 5in\cdot(y_t - 2.5in)^2 + 21.86in^4 + 21.44in^2\cdot(6.71in - y_t)^2 + \frac{\pi}{4}\cdot\left(\frac{5}{8}in\right)^2\cdot(n_s - 1)\cdot(4.18in - y_t)^2}{8in} \qquad I = 44.09\cdot\frac{in^4}{in}$$

Equivalent thickness for self-weight

$$t := \frac{\left(8in\cdot 5in + 21.44in^2 + 0.125in\cdot 8in\right)}{8in} \qquad t = 7.81\cdot in$$

POSITIVE BENDING CRACKED

Solve for ybar and I

Given $\quad y_{bar} := 0.5in \quad A_s := 0.31in^2 \quad d := 4.1875in$

$$8in\, y_{bar}\cdot\frac{y_{bar}}{2} - n_s\cdot A_s\cdot(d - y_{bar}) = 0$$

$$y_{bar} := Find(y_{bar}) \qquad y_{bar} = 1.31\cdot in$$

$$I := \frac{y_{bar}^3}{12} + y_{bar}\cdot\left(\frac{y_{bar}}{2}\right)^2 + n_s\cdot\frac{A_s}{8in}\cdot(d - y_{bar})^2 \qquad I = 3.224\cdot\frac{in^4}{in}$$

NEGATIVE BENDING CRACKED

Given $\quad y_{bar} := 0.5in \quad A_s := 0.31in^2 \quad d := 4.31in$

$$5.75in\, y_{bar}\cdot\frac{y_{bar}}{2} + \frac{6.5in - 5.75in}{3.5in}\cdot y_{bar}\cdot\frac{y_{bar}}{2}\cdot y_{bar}\cdot\frac{1}{3} - n_s\cdot A_s\cdot(d - y_{bar}) = 0$$

$$y_{bar} := Find(y_{bar}) \qquad y_{bar} = 1.51\cdot in$$

$$I := \frac{6.7179in^4}{8in} + n_s\cdot\frac{A_s}{8in}\cdot(d - y_{bar})^2 \qquad I = 3.181\cdot\frac{in^4}{in}$$

Say I = 3.2 in^4/in both ways

LONGITUDINAL

UNCRACKED

$$I_{long} := \frac{(5in)^3}{12} = 10.42\cdot\frac{in^4}{in} \qquad A_{long} := 5in = 5.00\cdot\frac{in^2}{in}$$

Given $\quad y_{bar} := 0.5in \quad A_s := 0.11in^2 \quad d := 3.6875in$

$$16in\, y_{bar}\cdot y_{bar} - n_s\cdot A_s\cdot(d - y_{bar}) = 0$$

$$y_{bar} := Find(y_{bar}) \qquad y_{bar} = 0.42\cdot in$$

C:\Documents and Settings\joshua.clapp\Desktop\Arch Decking Calcs.xmcd

This test report shall not be reproduced, except in full, without the written approval of the AEWC Advanced Structures & Composites Center.

Page: 3
By: JDC Date: 5/2/2011
Checked by: ____ Date: 5/2/2011

LONGITUDINAL (continued)

POSITIVE BENDING CRACKED

$$I_{pos} := \frac{y_{bar}^3}{12} + y_{bar}\cdot\left(\frac{y_{bar}}{2}\right)^2 + n_s\cdot\frac{A_s}{16in}\cdot(d - y_{bar})^2 \qquad I_{pos} = 0.592\cdot\frac{in^4}{in}$$

Given $y_{bar} := 0.5in$ $A_s := 0.11in^2$ $d := 1.3125in$

$$16in\, y_{bar}\cdot y_{bar} - n_s\cdot A_s\cdot(d - y_{bar}) = 0$$

$$y_{bar} := \mathrm{Find}(y_{bar}) \qquad y_{bar} = 0.24\cdot in$$

NEGATIVE BENDING CRACKED

$$I_{neg} := \frac{y_{bar}^3}{12} + y_{bar}\cdot\left(\frac{y_{bar}}{2}\right)^2 + n_s\cdot\frac{A_s}{16in}\cdot(d - y_{bar})^2 \qquad I_{neg} = 0.066\cdot\frac{in^4}{in}$$

FRP decking - CP155

$$n_{FRP} := \frac{4200ksi}{E_c} \qquad n_{FRP} = 1.12$$

$$I_{FRP} := \frac{11.16in^4}{ft} \qquad I_{FRP} = 0.93\cdot\frac{in^4}{in}$$

$$A_{FRP} := \frac{3.64in^2}{ft} \qquad A_{FRP} = 0.30\cdot\frac{in^2}{in}$$

$$wt_{FRP} := 3.75psf \qquad t_{eq} := \frac{3.75psf}{145pcf} \qquad t_{eq} = 0.31\cdot in$$

Arch Moment of Inertia

Effective diameter for EI calculation $d := 11.8in$

Uncracked $I_{uncracked} := \frac{\pi\cdot d^4}{64} = 951.70\cdot in^4$

$$EI_{uncracked} := E_c\cdot I_{uncracked} = 3.58\times 10^6\cdot kip\cdot in^2$$

Cracked $EI_{cracked} := \frac{669.21kip\cdot in}{\frac{0.000911}{in}} = 7.35\times 10^5\cdot kip\cdot in^2$

Ratio uncracked to cracked $\frac{EI_{uncracked}}{EI_{cracked}} = 4.87$

Ratio arch to concr. deck M+ $\frac{EI_{cracked}}{I_{pos}\cdot E_c\cdot 60in} = 5.51$

Ratio arch to concr. deck M- $\frac{EI_{cracked}}{I_{neg}\cdot E_c\cdot 60in} = 49.58$

C:\Documents and Settings\joshua.clapp\Desktop\Arch Decking Calcs.xmcd

This test report shall not be reproduced, except in full, without the written approval of the AEWC Advanced Structures & Composites Center.

APPENDIX B: COMPRESSION BOUNDARY PLATES

B.1. Under Layers

Under layers were used either to provide a rigid surface to increase the area of the crosshead or to provide a softer layer to help distribute the load on the specimen. The base layer was typically ½in steel plate with a 11.8in by 18.8in area (see Figure B.1), but for testing larger diameter specimens and some of the subsequent 6.5in specimens a 5 layer built up 3.74inthick by 18.8in per side plywood plate was used to increase the area of the crosshead, as in Figure B.2.

With both resin caps and plywood plates, 0.236in neoprene was sometimes used as a distribution layer where differential crushing of the neoprene would more evenly distribute the load. This technique is used in the testing of concrete cylinders. Results indicated that neoprene gave no improvement-specimens with neoprene still had uneven strains and were as likely to undergo resin cracking prior to tube buckling. Figure B.1 and Figure B.2 show typical boundaries using a neoprene distribution layer.

Figure B.1. Resin Cap with Neoprene Distribution Layer and Steel Base

This test report shall not be reproduced, except in full, without the written approval of
the AEWC Advanced Structures & Composites Center.

Figure B.2. Wood Plate with Neoprene Distribution Layer and Wood Base

B.2. Steel Bearing Plates

When steel was used in direct contact with the specimen the specimen failed in bearing as observed in testing during the summer of 2009 as well as specimen 6-3.

Figure B.3. Specimen Crushed by Direct Contact with Steel Bearing Plate

This test report shall not be reproduced, except in full, without the written approval of
the AEWC Advanced Structures & Composites Center.

The high bending stiffness of the thick steel plate and the high elastic modulus of the steel (greater than the specimen) allowed for insufficient movement at the boundary interface and localized contact caused a delamination failure on the end of the tube.

B.3. Resin Caps

Approximately 12mm thick resin caps were cast onto the top and bottom face of the specimen to generate even boundaries. The caps were parallel to each other, but in many cases they were not flat because the heat of resin curing caused the cap to warp as it was forming. Caps were shaped by flat-sided glass moulds with concave sidewalls treated with a mold release to allow easy removal of resin. A piece of chopped strand glass fiber matting was placed into the resin to limit thermal shrinkage cracking. During curing the specimen was suspended approximately 6mm above the glass plate to center the specimen within the resin.

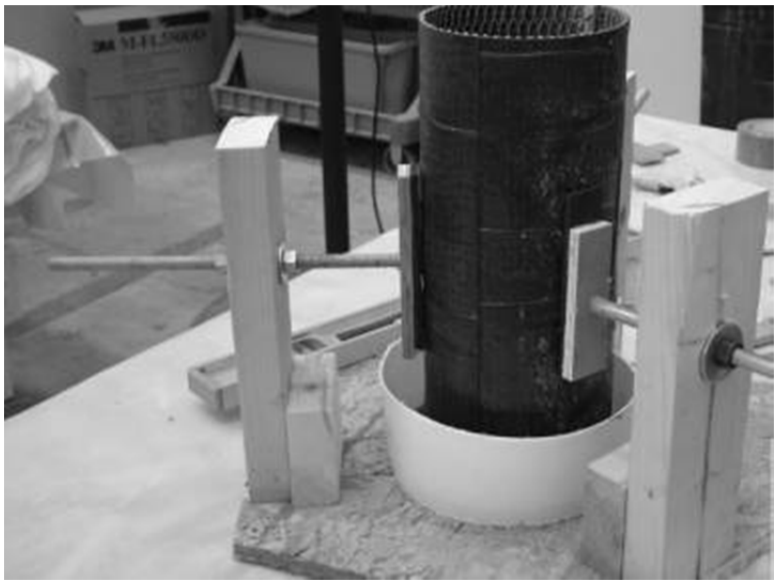

Figure B.4. Specimen in Resin Capping Stand

During loading, resin caps frequently fractured before the specimen failed; a series of loading and unloading ensued that decreased the accuracy of the strain measuring instruments and caused uneven loading conditions leading to early failure.

This test report shall not be reproduced, except in full, without the written approval of
the AEWC Advanced Structures & Composites Center.

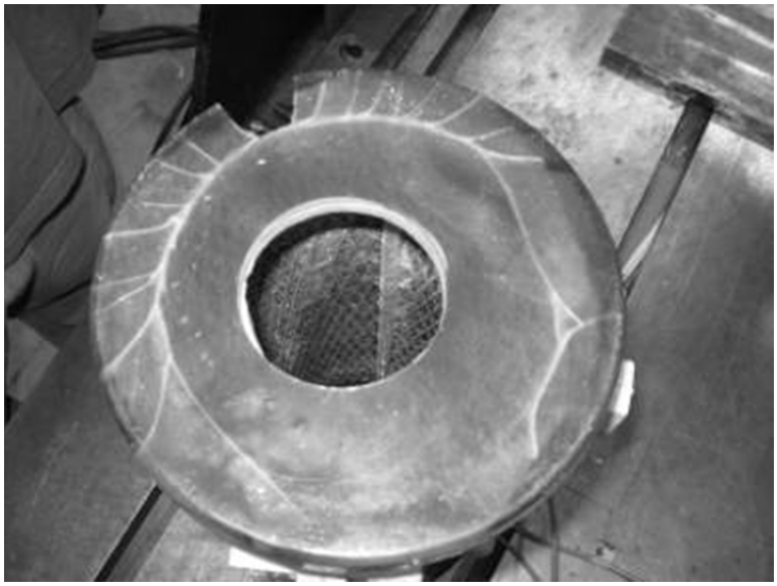

Figure B.5. Cracked Resin Cap After Loading

Resin caps also allowed several specimens to fail in sudden buckling, but the resin caps were higher cost, one time use, time consuming to manufacture, and produced many specimens that could not be counted for ultimate strength. With unlimited time and access to materials, resin caps may produce the best boundary. For this lab trial, resin caps proved difficult to implement.

B.4. Plywood Bearing Plates

Plywood was used as the boundary plate for all tests in 2009 and many tests in 2010, becoming the preferred boundary for future testing. Testing in 2009 employed ½" CDX pine plates reused for all specimens. These plates became heavily grooved after a single test and in subsequent tests may have contributed to the uneven load distributions measured on the specimen and indicated by the failure type.

Figure B.6. Plywood Cap on a 300mm Specimen

This test report shall not be reproduced, except in full, without the written approval of
the AEWC Advanced Structures & Composites Center.

Imperfections in the wood such as initial curvature or knots and other inclusions may have contributed to uneven loading conditions. To correct this issue the plywood used in 2010 was a ¾"cabinet grade hardwood with lower curvature and cleaner faces with fewer knots. Wooden plates were only used twice – once on each side – to ensure that specimens were not loaded unevenly due to existing grooves.

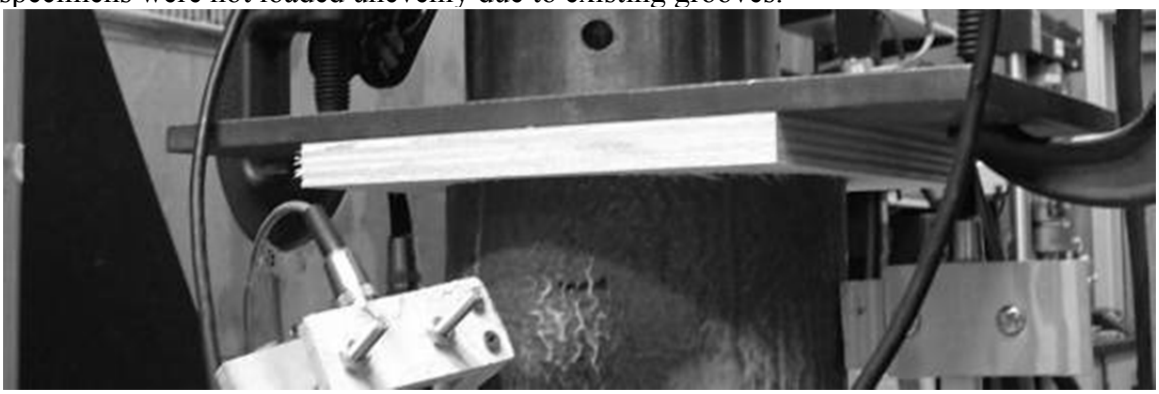

Figure B.7. Higher Grade Plywood Boundary

The plywood did not eliminate all uneven loading conditions but it did help uneven boundaries by crushing (differentially based on load) prior to specimen failure. Typical crushing began at 40% of max load for single layer samples and 20% of max load for other samples. Many specimens tested with wood boundaries show a single gauge taking a large amount of deflection initially that slows down after the wood begins crushing while other gauges take on additional deflection.

B.5. FRP Bearing Surface on Plywood

Plywood served as a good boundary for the larger diameter samples and the single layer specimens, but as the failure load became higher the plywood experienced large crushing deformations and the specimen failed in buckling-bearing failure. This failure mode is a buckling failure that occurs on an extreme edge of the specimen between the instrumentation and the plate. This failure initiates as a material wrinkle, but it suggests that the failure is influenced by the proximity of the load source. To correct this problem for stronger specimen types a plate was needed between the plywood that had a higher cutting strength, but was flexible enough to move with the plywood underneath as the plywood crushed. Two layers of braided carbon FRP (0.03in, +/-22 deg) arranged in opposite directions (strong axis of one lamina was placed against the weak axis of the other lamina) served as the bearing surface. During testing, the specimen damaged the FRP, breaking the matrix, but not breaking the fibers.

This test report shall not be reproduced, except in full, without the written approval of
the AEWC Advanced Structures & Composites Center.

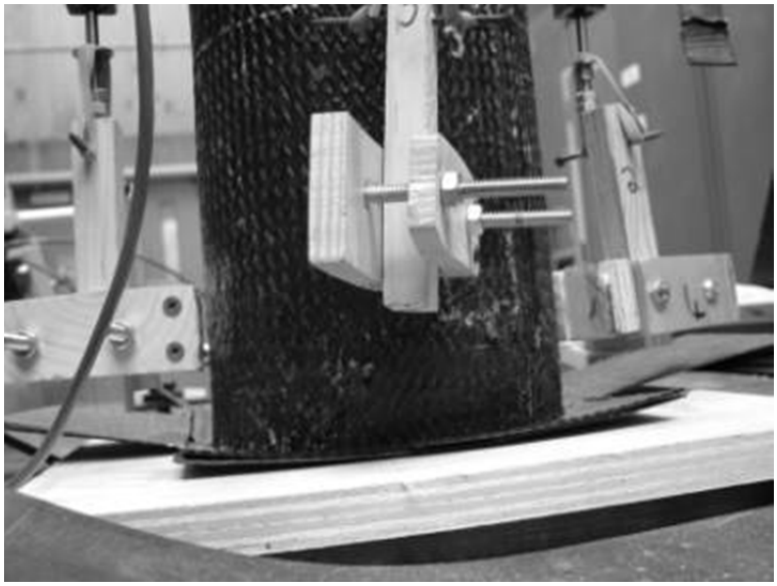

Figure B.8. FRP Plate with Plywood Sandwich Plate

The FRP bent around the specimen as it was forced into the plywood. The plywood groove from this test is both wider and shallower from those of similar load capacities performed without FRP covering. It resembled a dent instead of a cut.

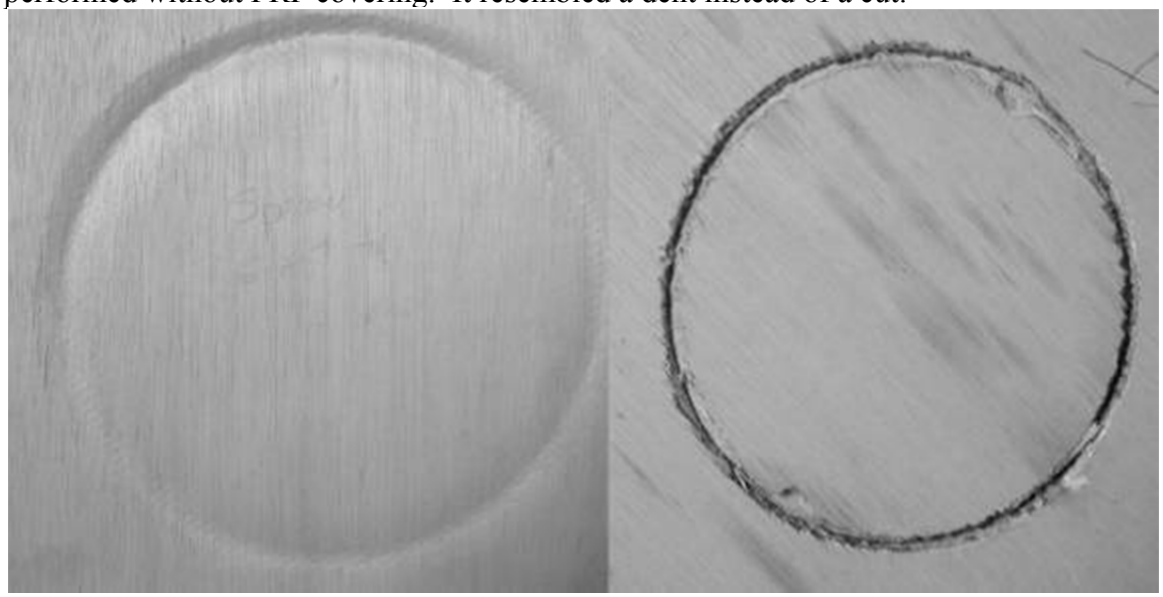

Figure B.9. Wood Core With FRP Without FRP

This test report shall not be reproduced, except in full, without the written approval of
the AEWC Advanced Structures & Composites Center.